

Research  
Frontiers of Chemical Engineering—Review

## Intermolecular and Surface Interactions in Engineering Processes

Jiawen Zhang, Hongbo Zeng\*

Department of Chemical and Materials Engineering, University of Alberta, Edmonton, AB T6G 1H9, Canada



### ARTICLE INFO

#### Article history:

Received 29 March 2020

Revised 18 July 2020

Accepted 20 August 2020

Available online 9 December 2020

#### Keywords:

Intermolecular and surface interactions

Colloids

Emulsions

Interface science

Engineering processes

Atomic force microscopy

Surface forces apparatus

### ABSTRACT

Interactions involving chemical reagents, solid particles, gas bubbles, liquid droplets, and solid surfaces in complex fluids play a vital role in many engineering processes, such as froth flotation, emulsion and foam formation, adsorption, and fouling and anti-fouling phenomena. These interactions at the molecular, nano-, and micro scale significantly influence and determine the macroscopic performance and efficiency of related engineering processes. Understanding the intermolecular and surface interactions in engineering processes is of both fundamental and practical importance, which not only improves production technologies, but also provides valuable insights into the development of new materials. In this review, the typical intermolecular and surface interactions involved in various engineering processes, including Derjaguin–Landau–Verwey–Overbeek (DLVO) interactions (i.e., van der Waals and electrical double-layer interactions) and non-DLVO interactions, such as steric and hydrophobic interactions, are first introduced. Nanomechanical techniques such as atomic force microscopy and surface forces apparatus for quantifying the interaction forces of molecules and surfaces in complex fluids are briefly introduced. Our recent progress on characterizing the intermolecular and surface interactions in several engineering systems are reviewed, including mineral flotation, petroleum engineering, wastewater treatment, and energy storage materials. The correlation of these fundamental interaction mechanisms with practical applications in resolving engineering challenges and the perspectives of the research field have also been discussed.

© 2020 THE AUTHORS. Published by Elsevier LTD on behalf of Chinese Academy of Engineering and Higher Education Press Limited Company. This is an open access article under the CC BY-NC-ND license (<http://creativecommons.org/licenses/by-nc-nd/4.0/>).

### 1. Introduction

Intermolecular and surface interactions play a critical role in a wide range of industrial interfacial processes, such as bubble attachment, emulsion stabilization and coalescence, flocculation and coagulation, fouling and scaling phenomena, and wastewater treatment [1]. The studies on related intermolecular and surface interactions can improve the understanding of the fundamental working principles determining the gas/oil/water/solid interfacial interaction behaviors, which facilitates the modulation of related engineering processes and boosts production efficiency [2–5]. For example, in the petroleum industry, asphaltenes adsorbed at a water/oil interface can stabilize water-in-oil (W/O) or oil-in-water (O/W) emulsions, resulting in oil–water separation difficulties, and pipeline fouling and corrosion. The surface interactions of emulsion droplets in oil production are complex due to the presence of other interface-active components (e.g., fine solid particles,

natural surfactants, and polymer additives), which are determinative in influencing emulsion stability. Understanding these interaction mechanisms are beneficial for resolving the technical challenges related to emulsions and asphaltenes in petroleum production. In mineral flotation, the selective bubble attachment to the particles of desired mineral species, instead of gangue minerals, is critical for effective separation of minerals. The selective attachment can be achieved by carefully regulating the interactions between air bubbles and mineral particles as well as by modulating the surface chemistry of mineral particles through addition of certain chemical additives (e.g., activators, collectors, or depressants) and water chemistry (e.g., pH, salinity). Therefore, understanding of the intermolecular and surface interactions involved in various engineering processes is of both fundamental and practical importance.

Tremendous efforts have been devoted to deciphering the intermolecular and surface interactions involved in various materials systems and engineering processes, including van der Waals (VDW), electrostatic interactions (e.g., ionic, hydrogen bonding, electrical double-layer (EDL) interaction), steric effects, solvation

\* Corresponding author.

E-mail address: [hongbo.zeng@ualberta.ca](mailto:hongbo.zeng@ualberta.ca) (H. Zeng).

interactions (e.g., hydration, hydrophobic and structural interactions), and so on. For example, VDW interactions exist among all substances. Under low salinity conditions, EDL repulsion prevents fine solids from aggregation and stabilizes solid particle suspensions. Increasing salinity greatly compresses the EDL, and thus the attractive VDW interaction dominates the surface interaction behavior of the solid particles [6,7]. In this review, the intermolecular and surface interactions commonly involved in the engineering processes are first introduced. The working principles of common force measurement techniques, namely, atomic force microscopy (AFM) and surface forces apparatus (SFA), are then briefly introduced. Our recent advances in deciphering the intermolecular and surface interaction mechanisms by using AFM and SFA are reviewed, with useful implications in several engineering fields, including mineral flotation, petroleum engineering, wastewater treatment, and energy storage materials. The correlation among the interaction mechanisms, novel functional materials fabrication, and the practical application performance in these systems are elucidated. Some remaining challenges and future perspectives are also discussed.

## 2. Intermolecular and surface interactions

In this section, some common intermolecular and surface interactions are briefly introduced, such as the VDW and EDL interactions, together known as the classical Derjaguin–Landau–Verwey–Overbeek (DLVO) interactions. Non-DLVO interactions, including hydrophobic force, steric force, depletion force, polymer bridging interaction, and hydration force, are also discussed. Fig. 1 shows the illustration of common DLVO and non-DLVO forces between particles or surfaces.

### 2.1. Van der Waals interactions

VDW interactions originate from the correlated fluctuating electric dipole moments of two molecules while they are

approaching each other, including induction, orientation, and dispersion forces, thus VDW forces are omnipresent between all molecules and surfaces [6]. The expressions of VDW interaction energies and forces between two bodies of different geometries with separation  $D$  in terms of Hamaker constant  $A$  are summarized in Table 1 [8].  $C_{VDW}$  is the VDW constant relevant to the polarizabilities of the two interacting molecules/bodies, and the dielectric permittivity of the medium.  $C_{VDW}$  equals to the summation of Debye induction constant  $C_{ind}$ , Keesom orientation constant  $C_{orient}$  and London dispersion  $C_{disp}$ .

Based on Lifshitz theory of VDW forces, the macroscopic bodies are treated as continuous media by neglecting the atomic structure. The nonretarded Hamaker constant  $A$  can be approximately expressed in terms of bulk properties (i.e., refractive indices  $n$  and dielectric permittivities  $\epsilon$ ). As shown in Eq. (1), for any systems including two interacting macroscopic bodies (1 and 2) across a media (3) with small separation, by assuming same absorption frequency for the three phases,  $A_{123}$  can be expressed as

$$A_{132} = A_{v=0} + A_{v>0} \approx \frac{3}{4}kT \left( \frac{\epsilon_1 - \epsilon_3}{\epsilon_1 + \epsilon_3} \right) \left( \frac{\epsilon_2 - \epsilon_3}{\epsilon_2 + \epsilon_3} \right) + \frac{3h_p \nu_e}{8\sqrt{2}} \frac{(n_1^2 - n_3^2)(n_2^2 - n_3^2)}{(n_1^2 + n_3^2)^{1/2}(n_2^2 + n_3^2)^{1/2} [(n_1^2 + n_3^2)^{1/2} + (n_2^2 + n_3^2)^{1/2}]} \quad (1)$$

where, the former component  $A_{v=0}$  represents entropic zero-frequency contribution, while the latter component  $A_{v>0}$  represents dispersion energy contribution;  $k$  is the Boltzmann constant;  $T$  is temperature;  $h_p$  is Planck's constant; and  $\nu_e$  is the maximum electronic ultraviolet adsorption frequency.

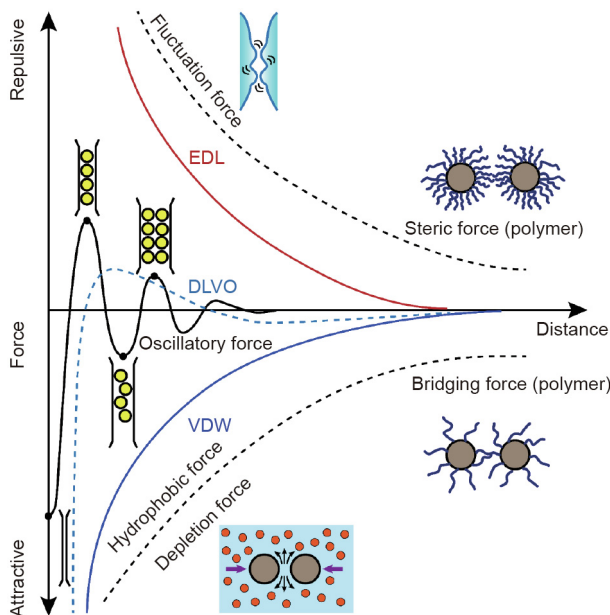
If the two interacting phases (1) across media (3) are the same, then the approximation of  $A$  can be simplified as

$$A_{131} \approx \frac{3}{4}kT \left( \frac{\epsilon_1 - \epsilon_3}{\epsilon_1 + \epsilon_3} \right)^2 + \frac{3h_p \nu_e}{16\sqrt{2}} \frac{(n_1^2 - n_3^2)^2}{(n_1^2 + n_3^2)^{3/2}} \quad (2)$$

These equations suggest that ① for two identical interacting phases across a medium,  $A$  is always positive and thus as shown in Table 1,  $F$  is always negative, namely, attractive; ② when the interacting macroscopic phases in a media are different,  $A$  can be positive or negative, suggesting attractive or repulsive  $F$ , respectively; ③ because for vacuum/air,  $\epsilon_3 = 1$  and  $n_3 = 1$ , thus for any two condensed phases in air/vacuum, the VDW force is always attractive.

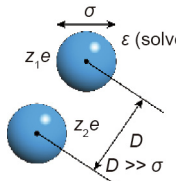
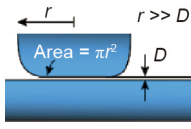
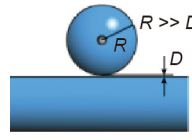
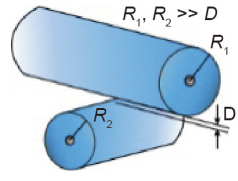
### 2.2. Electrostatic forces

Only in some limited cases, for example, the wetting behavior of nonpolar films on solid surfaces, the VDW interactions dominate the interaction behavior alone. While when aqueous solutions are involved as one media, the long-range electrostatic forces, in most cases, participate in the surface interactions, and its interplay together with the VDW interactions should be taken into consideration. For charged surfaces in water, an EDL would form in the vicinity of the charged surfaces. Different models were developed to describe the EDL, such as Helmholtz, Gouy–Chapman, and Stern models. The electrostatic potential and charge density in the vicinity of the surface are correlated by the Poisson equation, and the spatial distribution of the ions in the EDL is given by the Boltzmann statistics. The Poisson–Boltzmann equation describes the electrostatic potential in the EDL. For particles carrying the same charge, the EDL surface interactions are repulsive, preventing the aggregation and precipitation of the particles. The EDL interaction energies,  $W_{EDL}(D)$ , for two similar phases of different



**Fig. 1.** Force–distance profiles between particles/surfaces with various interactions possibly involved in the engineering processes. The sign of VDW interaction depends on the varieties of interacting media. EDL interaction is repulsive or attractive between particles/surfaces of the same or opposite charges, respectively. The classical DLVO forces include VDW and EDL interactions. Typical non-DLVO interactions include steric force, solvation forces (e.g., hydrophobic, hydration, and oscillatory structural interactions), polymer bridging interaction, and depletion interaction.

**Table 1**  
The expressions of VDW and EDL interaction energies and forces between two bodies of different geometries with separation  $D$  in terms of Hamaker constant  $A$  [8].

Item	Two atoms or small molecules	Two flat surfaces	Sphere (radius $R$ ) and a flat surface	Two orthogonal rods/cylinders (radii $R_1$ and $R_2$ )
Geometry of bodies with separation $D$ ( $D \ll R$ )				
VDW interaction				
$W_{VDW}(D)$	$-C_{VDW}/D^6$	$W_{VDW,plane} = -A/(12\pi D^2)$	$-AR/(6D)$	$-A\sqrt{R_1R_2}/(6D)$
$F_{VDW}(D)$	$-6C_{VDW}/D^7$	$-A/(6\pi D^3)$	$-AR/(6D^2) = 2\pi RW_{VDW,plane}$	$-A\sqrt{R_1R_2}/(6D^2) = 2\pi\sqrt{R_1R_2}W_{VDW,plane}$
EDL interaction				
$W_{EDL}(D)$	$\frac{+z_1z_2e^2}{4\pi\epsilon_0D} \frac{e^{-\kappa(D-\sigma)}}{1+\kappa\sigma}$	$W_{EDL,plane} = [\kappa/(2\pi)]Ze^{-\kappa D}$	$RZe^{-\kappa D}$	$\sqrt{R_1R_2}Ze^{-\kappa D}$
$F_{EDL}(D)$	$\frac{+z_1z_2e^2}{4\pi\epsilon_0D^2} \frac{1+\kappa D}{1+\kappa\sigma} \times e^{-\kappa(D-\sigma)}$	$[\kappa^2/(2\pi)]Ze^{-\kappa D}$	$\kappa RZe^{-\kappa D} = \pi RW_{EDL,plane}$	$\kappa\sqrt{R_1R_2}Ze^{-\kappa D} = 2\pi\sqrt{R_1R_2}W_{EDL,plane}$

VDW interaction energy  $W_{VDW}(D)$  and force  $F_{VDW}(D) = -dW_{VDW}/dD$  in terms of Hamaker constant  $A$ .  $C_{VDW}$  is the VDW constant. EDL interaction energy  $W_{EDL}(D)$  and force  $F_{EDL}(D) = -dW_{EDL}/dD$  in terms of interaction constant  $Z$ , between two phases with various geometries. Negative  $F$  suggests attractive force, while positive  $F$  implies repulsive force. The expression for  $A$  is described by Eq. (1).  $Z$  is defined by Eq. (3).  $1/\kappa$  is the Debye length.

geometries in aqueous media, under the assumption of constant surface potential, can be expressed in terms of an interaction constant  $Z$ , the dimensions of the interacting objects, and Debye length  $1/\kappa$ , as summarized in Table 1. The constant  $Z$  ( $J \cdot m^{-1}$  or  $N$ ) for EDL interactions is analogous to the Hamaker constant  $A$  for VDW interactions, defined by

$$Z = 64\pi\epsilon_0\epsilon \left(\frac{kT}{ze}\right)^2 \tanh^2\left(\frac{ze\psi_0}{4kT}\right) \quad (3)$$

where  $\epsilon_0$  and  $\epsilon$  represent the dielectric permittivity of the free space and medium, respectively;  $z$  is the electrolyte valence; and  $\psi_0$  stands for the surface potential. For a monovalent 1:1 electrolyte (e.g., NaCl),  $Z$  can be expressed as  $Z = 9.22 \times 10^{-11} \tanh^2(\psi_0/130) J \cdot m^{-1}$  at 25 °C, where  $\psi_0$  is in units of mV. Eq. (3) shows that  $Z$  is affected by the surface properties and the valence of electrolyte in solution. Debye length  $1/\kappa$  represents the decay length of the double-layer interaction, which depends on temperature, the electrolyte type, and concentration. With increasing concentration and valence of the ions,  $1/\kappa$  decreases.

The classical DLVO theory has been widely applied to describe the stability of colloidal particles in aqueous media, which includes both VDW and EDL interactions. As shown in Table 1, the DLVO forces, as a function of separation distance, can be either attractive or repulsive, depending on the surface properties and solution conditions [9].

### 2.3. Non-DLVO interactions

Besides VDW and EDL interactions, several other interactions, such as hydrophobic effects, steric force, depletion force, polymer bridging interaction, and hydration force, can also significantly influence the interactions of molecules and surfaces in related material systems or engineering processes, but cannot be described by the classical DLVO theory. These interactions are generally referred as non-DLVO interactions. For example, hydrophobic interactions were found to drive the aggregation of hydrophobic moieties in aqueous media, regulating the macromolecular or biomolecular conformation [10], froth flotation [11], micelle formation [12], and oil–water separation [13]. In 1982, for the first time, a long-range attractive force, much stronger than VDW interaction, was directly measured by Israelachvili and Pashley between two hydrophobic surfaces in aqueous solutions [14]. This hydrophobic interaction was found to decay exponen-

tially and the characteristic length was determined as  $\sim 1$  nm. Since then, much effort has been devoted to investigate the hydrophobic interactions in different material systems, but its origin is still not fully understood. The possible mechanisms for the reported long-range attraction between hydrophobic surfaces include bridging of surface nano-/micro-bubbles [15–17], bubble cavitation during surface approaching or separation [18–20], or entropy elevation due to the disruption and change of hydrogen bonding network at the water–hydrophobic interface [21].

When polymers are present at solid–liquid interfaces, a repulsive entropic force would generally occur due to the compression of polymer chains during the approaching of two surfaces, which is known as the steric force [8,22,23]. The surface groups of polymers and the easily deformable interfaces (e.g., gas–liquid, liquid–liquid interfaces) always undergo thermal motions. During the approaching of two surfaces, the fluctuation range of these thermal motions would be generally restricted, leading to entropic thermal fluctuation force [24,25]. For surfaces adsorbed with relatively low amounts of polymers, the free end of a polymer bound to one surface may physically bind to another surface, thus adhesive bridging force arises between the two surfaces [22,26]. If the polymers are not chemically/physically bound to any surface but freely exist in the solution, when two surfaces are brought close to each other, a “depletion zone,” namely, a zone with no polymer existing, will occur between the two surfaces [22,27]. The polymer concentration difference between the bulk polymer solution and the depletion zone would lead to an osmotic pressure difference, which would result in the migration of water molecules from the depletion zone to the bulk solution, leading to a depletion force which drives the surfaces to move closer.

For hydrophilic surfaces in aqueous media, hydration force exists between the interacting surfaces in short distance range due to the steric hindrance of hydrated ions binding to the charged surfaces. The hydration force could be monotonically repulsive, oscillatory or overall repulsive but showing oscillatory behavior at shorter distances. Hydration forces depend on the ion species and concentrations in the intervening liquid medium, surface roughness, and the location difference of the outer Helmholtz plane and physical solid–liquid interface [28–30].

### 3. Nanomechanical techniques

Various experimental techniques have been developed to characterize the intermolecular and surface interaction mechanisms by

directly measuring the interaction forces or energies involved, and the associated changes of surface deformation and morphology. One of the pioneering surface force measurements was performed by Derjaguin and his co-workers in early 1950s, when they measured the attractive force between glass surfaces in vacuum and attributed it to VDW interactions [31,32]. Since then, with the development of advanced nanomechanical tools, the interaction forces in various systems have been investigated, such as solid–solid interaction forces in gas, vapor with condensed liquid film or bulk liquid, gas bubble/liquid droplet–solid interaction forces, and gas bubble–gas bubble interaction forces in liquid solutions. The most straightforward approach to establish the force–distance profile is to measure the interaction forces while bringing two surfaces together and then apart. The developed approaches to measure forces with high precision commonly involve spring deflection, magnetic/electric field, osmotic/light pressure, viscous forces, and buoyancy forces [8]. By using the spring deflection approach, the interaction force  $F$  can be obtained via Hooke's law,

$$F = k_{\text{spring}}\Delta x \tag{4}$$

where  $k_{\text{spring}}$  is the spring constant and  $\Delta x$  is the spring deflection. In surface force measurements, curved surfaces are usually employed, and some typical configurations include sphere–plane surfaces, two sphere surfaces, and two crossed cylinder surfaces as depicted in Table 1. For curved surfaces, the contact area is much smaller compared with that between two flat surfaces, thus the preparation of dust-free surfaces will not be difficult. Besides, the alignment difficulty for curved surfaces is vastly reduced as compared with that for two parallel planes. The interaction energy per unit area between two flat surfaces  $W(D)_{\text{plane}}$  can be correlated to the interaction force  $F(D)$  measured between curved surfaces (e.g., two orthogonally crossed cylinders or a sphere with a flat surface) based on the Derjaguin approximation, when the separation distance  $D$  is much smaller than the radius of the curved surface  $R$ , as shown in Eq. (5) [8,33].

$$W(D)_{\text{plane}} = \frac{F(D)}{2\pi R} \tag{5}$$

Over the past few decades, various advanced nanomechanical techniques have been developed, such as the SFA, AFM, optical tweezers (OTs), magnetic tweezers (MTs), and Johnston–Kendall–Roberts (JKR) apparatus. The comparisons of several common force measurement techniques are summarized in Table 2 [34–39]. SFA and AFM are among the most commonly and widely employed force measurement techniques for probing the intermolecular and surface forces in diverse engineering processes and material systems, of which the working principles are introduced in details

below. Other nanomechanical tools such as OT and MT have also been applied to quantify the interaction forces of different materials. OT employs gradient lasers to trap and manipulate dielectric particles [6], while MT can manipulate paramagnetic beads through gradient magnetic field [39]. The force sensitivity of OT and MT is relatively higher than SFA and AFM, which are commonly applied in biological systems [34,39]. OT performs high time-dependent control of the applied forces, and can easily manipulate the particles [8,39]. One limitation of OT technique is that the sample heating, attributed to intense laser power, could occur during measurement and may damage the samples [6]. Via the MT technique, the control of multiple beads can be achieved simultaneously, but the main limitations of this technique are the hysteresis of magnetic field and the spatiotemporal resolution restricted by the video-based data acquisition, which recently has been improved by using high-speed camera [34,38,39].

### 3.1. Surface forces apparatus

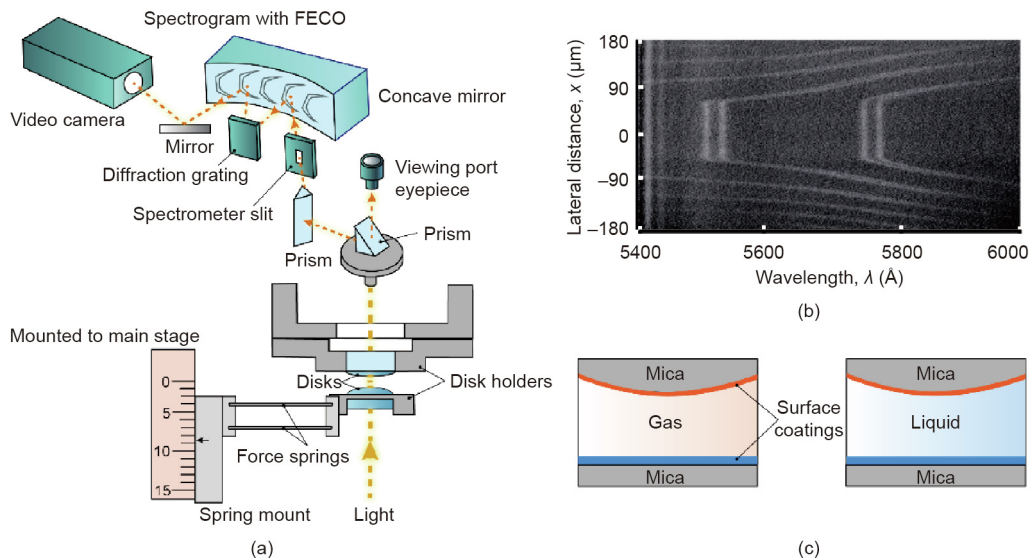
The SFA technique was first developed by Tabor, Winterton, and Israelachvili [40–42], in the late 1960s and early 1970s for measuring surface forces between atomically smooth mica surfaces in vacuum or gas. The SFA technique was then significantly advanced by Israelachvili by extending the surface force measurements to diverse liquid and vapor environments and a broad range of material systems and biological and engineering systems [8]. Many of the intermolecular and surface forces (DLVO and non-DLVO interactions) introduced in Section 2 were first measured by Israelachvili and his co-workers using the SFA.

Fig. 2(a) shows a typical experimental setup for force measurements using SFA. In a typical SFA experiment, two back-silvered thin mica sheets (~1–5 μm) are first glued on two cylindrical glass disks with radius  $R$ . The thickness of the back-silver coating is ~50 nm, which is required to obtain the multiple-beam interference fringes of equal chromatic order (FECO) for monitoring the surface separation, deformations, and contact area in real time and *in situ* (Fig. 2(b)). The two surfaces are mounted into the SFA chamber in a crossed-cylinder configuration, whose interaction is equivalent to a sphere of radius  $R$  interacting with a flat surface according to the Derjaguin approximation. Light is then generated by a white light source and directed to pass through the two surfaces. The interference light is directed to a spectrometer with diffraction grating, which is then recorded using a video camera. The normal forces between the two surfaces were measured by making the two surfaces to approach and separate from each other, then obtained using the Hooke's law. The deflection of the force spring is determined using the difference between the distance

**Table 2**  
The comparison of some common force measurement techniques [34–39].

Force measurement techniques	Force measurement mechanism	Force sensitivity (N)	Distance resolution (nm)	Features	Limitations
AFM	Spring deflection	$10^{-12}$ to $10^{-11}$	~0.1	Used for both imaging of high resolution and force measurements	Arbitrarily determined separation distance, especially for soft materials and highly deformable surfaces
SFA	Spring deflection	$< 10^{-8}$	< 0.1	Measuring absolute surface separation distance, with high resolution of interaction energy per unit area	Commonly requiring (semi)transparent samples with low surface roughness
OTs	Gradient in light intensity	$\sim 10^{-14}$	0.2	Easy manipulation and high time-dependent control	Potential photo-damage and sample heating
MTs	Magnetic field gradient	$10^{-15}$	1	High force sensitivity, manipulation of multiple beads	Hysteresis of magnetic field, spatiotemporal resolution limited by video-microscopy





**Fig. 2.** (a) Schematic of a typical experimental setup using an SFA for measuring the interaction forces  $F$  as a function of separation  $D$  between two surfaces in vapor or liquid media. The force is applied and measured by monitoring the deflection of force springs, as determined using the Hooke's law. (b) The surface separation, deformation, coating thickness, and contact area can be measured in real time using a multiple beam interferometry (MBI) by employing fringes of equal chromatic order (FECO). (c) The force measurements can be carried out for two surfaces interacting in vapors or liquid media in symmetric or asymmetric configurations.

driven and the actual distance that the two surfaces moved relative to each other as monitored by the multiple beam interferometry (MBI) by employing the FECO. As such, SFA can measure the force  $F$  between two curved surfaces with a sensitivity of  $< 10$  nN as a function of the absolute surface separation  $D$  of these two surfaces with a resolution of higher than 0.1 nm. SFA measurements generally possess relatively higher resolution of  $F/R$  or interaction energy per unit area as compared with that of AFM. The environmental conditions (e.g., temperature, pressure) of SFA measurements can also be well controlled. As illustrated in Fig. 2(c), the two opposing mica surfaces can be modified by various organic and inorganic coatings (e.g., silica, gold, oxides, surfactants, polymers, and proteins) in asymmetric or symmetric configurations, and the surrounding medium can be gas, vapor, aqueous solution, or organic solvent. The surfaces or films in SFA measurements are generally transparent or semitransparent with low surface roughness [8].

Besides the normal forces, SFA can be also applied to quantify the lateral forces between two surfaces in vapors or liquid media to study a wide range of friction, rheology, and lubrication phenomena at the nanoscale [9,43,44,36,45,46]. X-ray diffraction/spectroscopy, electrical field modulation, electrochemical control, and fluorescence imaging have been coupled to SFA, which has expanded the capacity of SFA to characterize the intermolecular and surface forces of various material systems [43,47–50].

### 3.2. Atomic force microscopy

In 1981, scanning tunneling microscopy (STM) was invented by Binnig et al. for atomic-level imaging for conductive and semiconductor surfaces [51]. Based on STM, AFM was further developed by Binnig, Quate, and Gerber from 1982 to 1986 for high-resolution topographic imaging of both conductive and insulating surfaces by modulating the forces between the AFM probe and sample surfaces [52,53]. Since then, AFM has been widely used for both imaging of high resolution and force measurements for numerous materials in vacuum, gas, and liquid media [54,55]. A typical setup of AFM experiments is illustrated in Fig. 3(a). In a force measurement, the tip probe on the AFM cantilever spring is driven toward and away from the sample substrate by the piezo. The interaction forces with piconewton sensitivity are determined via the Hooke's

law by monitoring the deflection of the cantilever spring, which is obtained from the displacement of a laser beam reflected on the back of the cantilever onto the quartered photodiode [36]. However, the separation distance obtained in AFM force measurement is generally arbitrarily determined, especially for soft materials and highly deformable surfaces. For topological imaging, the tip probe is driven to raster scan across the sample surface, and typically the force between tip and sample surface is controlled to be constant through a feedback loop. As such, the height of the sample surface on each raster point is recorded to obtain a 3-dimensional topographic profile.

Over the past three decades, several AFM tip probes have been developed and applied in force measurements for numerous materials and engineering systems, including nanoscale sharp tip (or surface functionalized tip), colloidal probe, bubble or drop probes, as illustrated in Figs. 3(b)–(d), respectively. The colloidal probe AFM technique allows force measurements between a colloidal probe and different substrates (Fig. 3(c)). A colloidal probe can be prepared by gluing a colloidal particle under one end of the tipless cantilever, and the diameter of the particle is typically around a few micrometers [56,57]. For the bubble probe (Fig. 3(d)), a typical preparation procedure is to first hydrophobize the circular gold patch under one end of the tipless AFM cantilever by immersion in absolute ethanol with  $10 \text{ mmol}\cdot\text{L}^{-1}$  dodecanethiol overnight. Gas bubbles are generated through an ultra-sharp glass pipet and immobilized on a mildly hydrophobized glass substrate. The hydrophobized AFM cantilever is lowered to attach a selected gas bubble (with typical radius  $\sim 50\text{--}100 \mu\text{m}$ ) and then elevated to lift the gas bubble. Afterwards, the gas bubble probe is laterally moved over a desired sample surface and ready for the force measurement. For the oil drop probe preparation, oil droplets are generated by a controlled dewetting method on mildly hydrophobized glass substrate to be lifted up by the strongly hydrophobized tipless probe cantilever [58]. For the water drop probe preparation, water is injected into organic solutions and the water droplets are settled on the highly hydrophobized glass substrate, which can be lifted up by the mildly hydrophobized cantilever [59]. The colloidal probe and gas/drop probe AFM techniques allow direct force measurements of a broad range of colloid particles, gas bubbles, and emulsions drops in complex fluids.

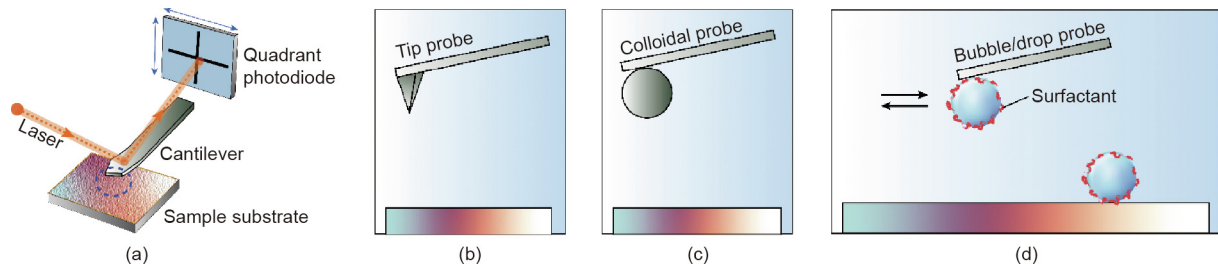


**Fig. 3.** (a) Schematic of a typical experimental setup of AFM for surface imaging and force measurement. The blue dash line circle highlights the probe location on the cantilever. (b)–(d) Typical AFM probes for force measurements: (b) nanoscale sharp tip, (c) colloidal probe, and (d) bubble/drop probe. The force measurements can be carried out in both air and liquid media depending on the variety of AFM probes and underlying substances.

**4. Applications of intermolecular and surface force measurements in engineering processes**

**4.1. Mineral flotation**

In mineral engineering, froth flotation is a key process to selectively collect desirable and valuable mineral particles, and the typical flotation process is illustrated in Fig. 4. Raw mineral ores are crushed and ground to liberate the desired components, which are further mixed with water containing conditioning reagents (e.g., collector, depressant). Air bubbles are then introduced to the mixture to capture the hydrophobic particles, which flow upwards together and form the froth, leaving the hydrophilic particles in the bulk mixture [59]. The bubble–mineral interaction is determinative in this flotation process, which can be affected by the interface-active reagents absorbed on the particle surface and aqueous conditions (e.g., hydrodynamic conditions, ion types, and concentrations) [11]. Thus, the comprehensive and fundamental understanding of the interactions among the solid mineral particles, air bubbles, and interface-active agents in aqueous media is significant in precisely modulating the related surface interactions in flotation processes and developing advanced interface-active reagents for improved separation efficiency.

To date, many studies have been carried out to investigate the underlying interaction mechanisms between air bubbles and mineral surfaces, among which the direct force measurements have

shown great promise by providing quantitative information on the bubble–mineral interaction mechanisms at the nanoscale. With the development of colloidal and bubble probe AFM techniques, AFM serves as one of the most widely used techniques to nanomechanically quantify the interaction forces between gas bubbles and solid surfaces in liquid media. For example, silica particles with different hydrophobicities have been used as model colloidal particles to probe the interactions with surface-immobilized bubbles [60–62]. While for many naturally occurring mineral particles (e.g., mica, molybdenite, sphalerite), their shapes are non-spherical, which could bring difficulties in the analysis and fitting of AFM experimental results measured using the colloidal probe AFM technique.

The bubble/drop probe AFM technique allows the direct force measurements between the cantilever-attached bubble or drop and a solid surface in liquid media, which shows certain advantages as compared to the conventional colloidal probe AFM technique, due to the relatively facile fabrication of flat mineral samples. For example, smooth and flat mica, molybdenite, and sphalerite surfaces can be readily prepared by cleavage, while flat chalcopyrite surface can be prepared by polishment [11,63–66]. By using the bubble probe AFM technique, the measured surface forces between air bubbles and solid surfaces were quantitatively reconstructed by using the Stokes–Reynolds–Young–Laplace theoretical model to theoretically calculate the bubble–solid separation (viz., confined thin water film thickness) [57]. However, the

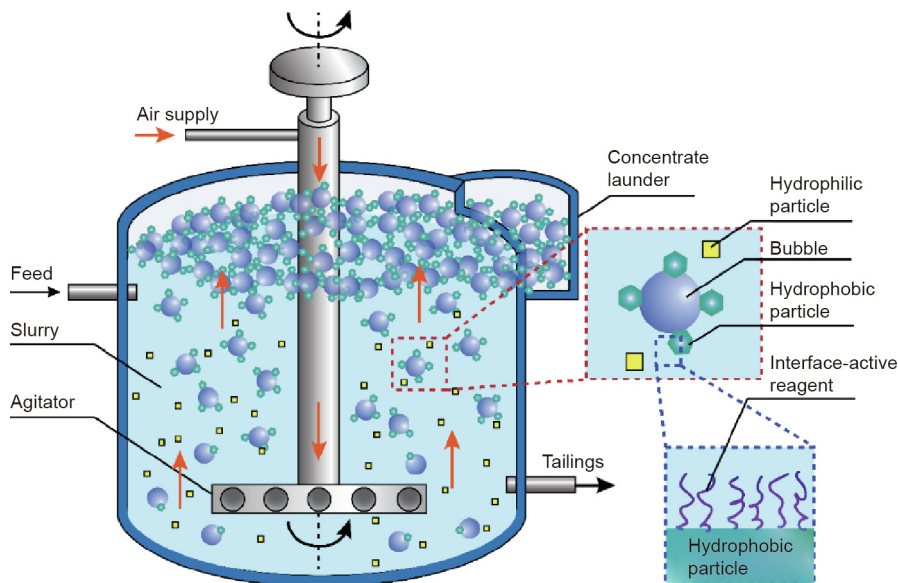


**Fig. 4.** Schematic diagram of a typical mineral flotation process. Hydrophobic particles attach to the rising air bubbles to be collected. The interface-active reagents adsorb on the mineral particles to modify their surface hydrophobicity and thus affect the flotation efficiency.

simultaneous measurements of the interaction force and separation distance between air bubbles and solid surfaces was still challenging mainly due to the deformation of gas bubbles. For the first time, reflection interference contrast microscopy (RICM) was implemented with the bubble probe AFM by Shi et al. [63] to achieve the synchronous measurement of the interaction forces and confined thin water film profile between air bubbles and a series of mica surfaces with various hydrophobicities. The typical experimental setup of AFM-RICM is shown in Fig. 5(a). The fringe patterns arising from the interference between the monochromatic light reflection at the interfaces of air bubble/water and water/mica can be obtained with RICM. Then the confined thin water film thickness,  $h(r, t)$ , can be determined by analyzing the order and light intensity of the interference fringe patterns to visualize the spatiotemporal evolution of the thin water film trapped between the air bubble and mica surface [67]. The AFM-RICM experiment results were found to agree well with the theoretical calculations based on the Stokes–Reynolds–Young–Laplace model by considering the effect of disjoining pressure, demonstrating the precise interpretation of underlying fundamental interaction mechanisms. The disjoining pressure  $\Pi_H(h)$  due to the hydrophobic interaction between air bubble and hydrophobized mica surface (e.g., Mica-octadecyltrichlorosilane (OTS)-90, static water-in-air contact angle,  $\theta_w$ , of  $90^\circ$ ) could be described by Eq. (6):

$$\Pi_H(h) = - \left[ \frac{\gamma(1 - \cos\theta_w)}{D_H} \right] \exp\left(-\frac{h}{D_H}\right) \quad (6)$$

where  $\gamma$  is the air–water surface energy,  $D_H$  is a characteristic decay length of hydrophobic interaction, and  $h$  represents the surface separation distance. As shown in Fig. 5(b), the force–time profile between the bubble and Mica-OTS-90 could be well fitted by the

theoretical calculation (red curve), with  $D_H$  determined as 1.0 nm. The attachment of the air bubble on the Mica-OTS-90 surface was attributed to the hydrophobic interaction since the VDW interaction for bubble–water–solid was repulsive, the EDL interaction was significantly suppressed under high salinity condition and the hydrodynamic interaction could be neglected under low approaching velocity. The fitted disjoining pressure was employed for calculating the thin water film profiles (solid curves) as shown in Fig. 5(c), which agreed well with the experiment results (open circles). The calculated critical thin water film thickness before bubble attachment was also consistent with the experimental measurement through RICM. As shown in Fig. 5(d), the air bubble attached to the hydrophobized mica surface when the magnitude of negative overall disjoining pressure was just over that of the Laplace pressure of the bubble. In this work, the bubble/drop probe AFM-RICM technique was proven as a useful tool for quantifying the bubble–solid surface interaction mechanisms.

Later on, the interactions of air bubbles with mineral surfaces (e.g., sphalerite, molybdenite, chalcopyrite) [11,64,66] and some other solid surfaces (e.g., polymers, bitumen, superhydrophobic surfaces) [68–70] were further quantitatively measured by using the bubble probe AFM technique. The underlying interaction mechanisms were deciphered, and the effect of solution salinity and pH as well as surface treatment (e.g., polymer adsorption) was thoroughly investigated [64,66,68,71]. For example, Xie et al. [66] investigated the interactions between air bubbles and molybdenite basal surface by using the bubble probe AFM technique (Fig. 6(a)). In the flotation process of copper–molybdenum ores, water-soluble polymers are commonly added to depress the bubble attachment to chalcopyrite, and the successful attachment of air bubbles to hydrophobic molybdenite would facilitate the

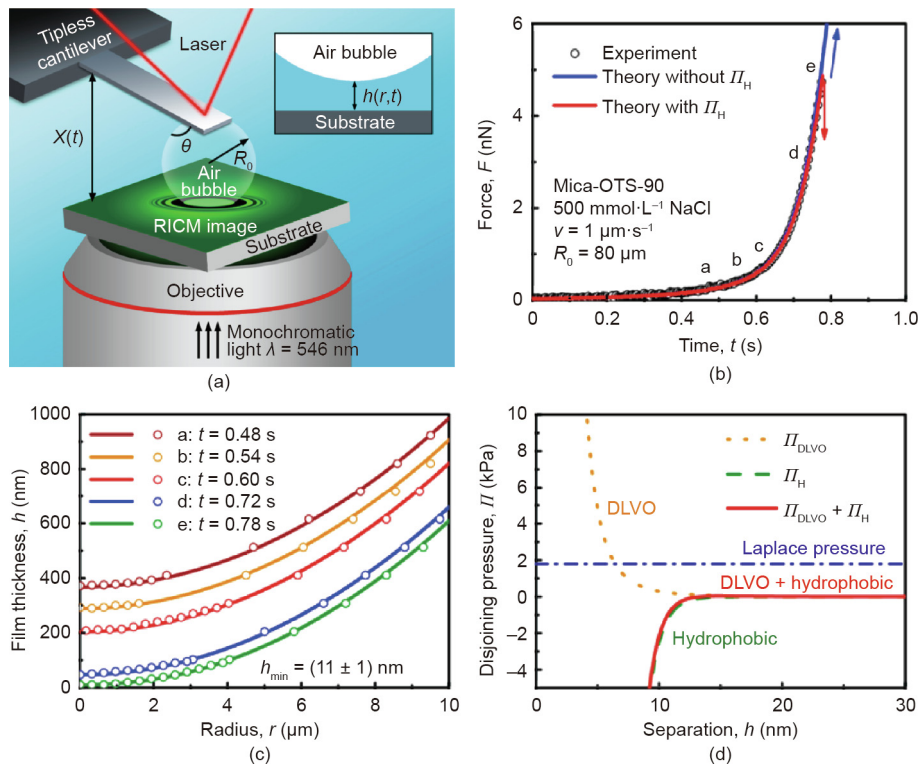


**Fig. 5.** (a) Schematic of experiment setup using bubble/drop probe AFM technique coupled with reflection interference contrast microscopy to simultaneously measure the interaction forces and spatiotemporal profiles of the confined thin water film between air bubbles and substrate surfaces of various hydrophobicities. (b) Force curves as a function of time between an air bubble and hydrophobized mica surface (water contact angle of  $90^\circ$ ) in  $500 \text{ mmol}\cdot\text{L}^{-1}$  NaCl. Red/blue solid curves: theoretical calculations with/without considering the hydrophobic disjoining pressure ( $\Pi_H$ ), respectively. Open circles: measured force data. (c) Water film profiles at different time intervals denoted as a–e in panel (b). Open circles: RICM measurement results. Solid curves: theoretical calculations. (d) Components of the disjoining pressure as a function of separation,  $h$ . Reproduced from Ref. [63] with permission of American Chemical Society, ©2015.



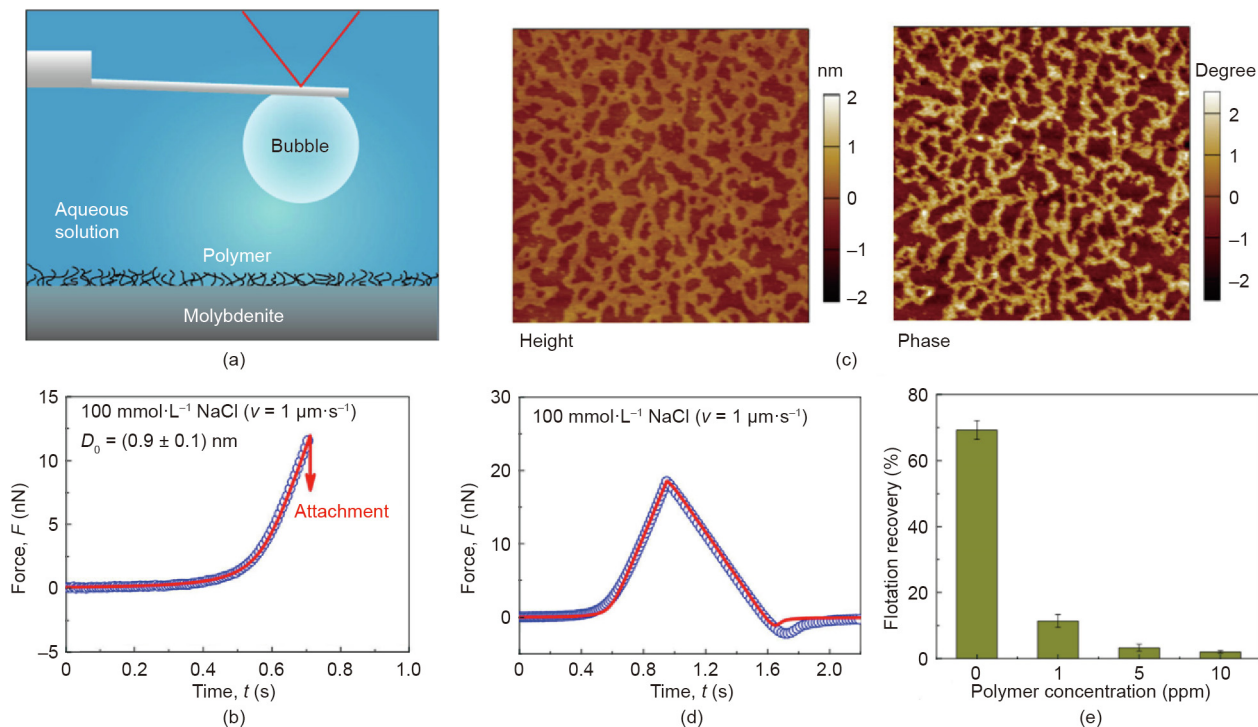


**Fig. 6.** (a) Schematic of surface force measurement between air bubble and polymer-conditioned molybdenite surface in aqueous solution by using the bubble probe AFM technique. (b) Interaction force curve between air bubble and molybdenite surface conditioned by 1 ppm guar gum solution. (c) AFM height and phase images of guar gum-conditioned (5 ppm) molybdenite surface (5  $\mu\text{m} \times 5 \mu\text{m}$ ). (d) Force curve between air bubble and guar gum-conditioned (5 ppm) molybdenite. (e) Effect of the guar gum concentration of the conditioning solution on the flotation recovery of molybdenite. Reproduced from Ref. [66] with permission of American Chemical Society, ©2017.

selective separation of molybdenite from the bulk mineral slurry. However, the added polymers could adversely adsorb on molybdenite surfaces, thereby increasing the surface hydrophilicity and decreasing the floatability of molybdenite [72]. In the work by Xie et al. [66], the effects of polymer conditioning time, polymer dosage, and electrolyte concentration on the adsorbed polymer (i.e., guar gum) coverage on the molybdenite surface as well as the effect of polymer coverage on the bubble attachment to molybdenite were systematically investigated. It was found that decreasing the NaCl concentration from 100 to 1 mmol·L<sup>-1</sup> could interfere with the bubble attachment by increasing the EDL repulsion. The hydrophobic interaction between air bubble and molybdenite surface in 100 mmol·L<sup>-1</sup> NaCl was demonstrated to be weakened after conditioning in 1 ppm guar gum, with the decay length of hydrophobic interaction dropping from 1.2 to 0.9 nm (Fig. 6(b)), and hence the bubble attachment became more difficult. With 5 ppm polymer conditioning, the polymer coverage on the molybdenite surface was ~44.5% based on AFM height and phase imaging results (Fig. 6(c)). During approaching of an air bubble to the treated molybdenite surface (conditioned with 5 ppm polymer) in 100 mmol·L<sup>-1</sup> NaCl aqueous solution, additional repulsion was detected on the interaction force curve (Fig. 6(d), open symbols). This additional repulsion was attributed to the steric repulsion arising from the extended polymer chains. Interestingly, with only ~44.5% coverage of polymer adsorbed on the molybdenite surface, the steric polymer repulsion together with the greatly depressed hydrophobic interaction were found to be sufficient to inhibit bubble attachment. The force measurement results were consistent with the flotation performances of molybdenite under a variety of treatment conditions (Fig. 6(e)). The validity of the bubble probe AFM technique in elucidating the bubble–mineral interaction mechanisms shows its promise to be readily extended to a broad range of other engineering processes. Bridging the fundamental understanding of the colloidal interaction behaviors with their

performances in practical flotation processes provides useful insights for the development of novel interface-active reagents and improving the related process efficiency.

In addition to the studies on the interactions between gas bubbles and mineral surfaces, the interactions between conditioning agents and mineral surfaces have also been measured using AFM in aqueous solutions. Typically, the AFM tip can be modified with conditioning agents and then used to investigate their intermolecular interactions and adhesion forces with mineral surfaces. Liu et al. [73] measured the interaction forces between hydroxamate-functionalized AFM tips and wolframite, calcite, and quartz surfaces (Fig. 7(a)). Hydroxamate acids are a commonly used class of collectors, which can facilitate the separation of mixed minerals via selectively adsorbing on certain minerals to enhance their surface hydrophobicity. The adhesion strength between the hydroxamate-functionalized AFM tip and wolframite surface was found to be higher than that between the AFM tip and calcite or quartz surface (Fig. 7(b)), which was ascribed to the strong binding of the hydroxamate group to the Fe atom on wolframite surface. The force measurement results were consistent with the flotation results (Fig. 7(c)). Furthermore, AFM can also be used with the implementation of an electrochemical setup. This allows the examination of the surface interactions between the AFM tip and mineral surfaces or the probing of the mineral surface morphologies by simultaneously modulating the interfacial electrochemical reaction of the electrochemically active mineral surfaces. Fig. 7(d) illustrates a typical experimental setup for performing topographic imaging and force measurements on the surface of electrochemically active galena mineral with the inset showing the geometry of the conical AFM tip [74]. The interaction forces between the OTS-functionalized AFM tip and galena surface were directly quantified. By increasing the potentials applied on the galena surface (i.e., from -0.7 to 0.45 V, referred to the Ag/AgCl/3.4 mol·L<sup>-1</sup> NaCl reference electrode), the magnitude of the



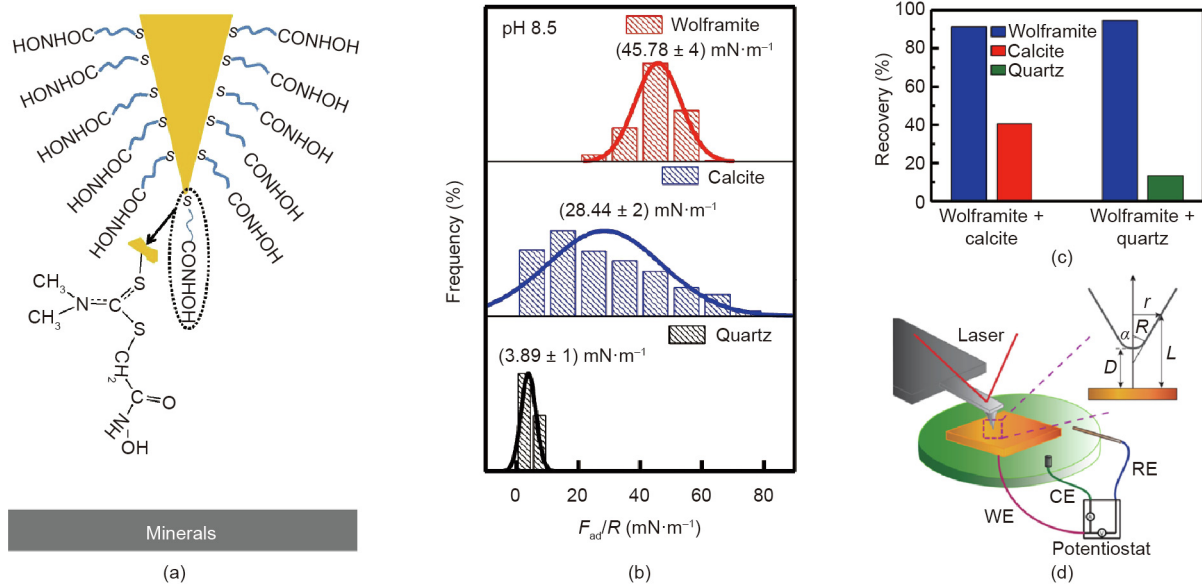


**Fig. 7.** (a) Schematic of surface force measurement between a hydroxamate-functionalized AFM tip and mineral surface. (b) The normalized adhesion force histograms between the hydroxamate-functionalized AFM tip and wolframite, calcite, and quartz surfaces in 1 mmol·L<sup>-1</sup> NaCl solution (pH 8.5). (c) Flotation recovery of the artificially mixed minerals in 0.2 mmol·L<sup>-1</sup> octyl hydroxamic acid solution (pH 8.5). (d) Schematic of AFM experiment implemented with electrochemical setup. RE: reference electrode; WE: working electrode; CE: counter electrode. (c) Reproduced from Ref. [73] with permission of Elsevier, ©2019; (d) reproduced from Ref. [74] with permission of American Chemical Society, ©2016.

hydrophobic interaction was found to increase due to the elevated surface hydrophobicity. The surface roughness of galena surface also increased with the homogenous oxidation. The fundamental understanding of surface interactions and topographic information of the electrochemically active mineral surfaces can provide useful implications for the mineral flotation process in terms of modulating the homo- and hetero-coagulation of mineral particles. Moreover, this methodology can be readily extended to investigate the interactions involved in many other engineering processes containing electrochemically active components.

#### 4.2. Petroleum engineering

With the gradual depletion of conventional crude oil, considerable efforts have been devoted to the efficient exploitation of unconventional heavy oil such as oil sands. Some of the challenges that need to be tackled in petroleum production include the stabilization/destabilization of O/W and W/O emulsions, fouling issues, oil/water separation, and tailings water treatment [35]. Asphaltenes are the heaviest fraction in petroleum fluids, defined as a class of compounds insoluble in light *n*-alkane solvents such as *n*-heptane but soluble in aromatic solvents like toluene. Asphaltenes tend to form nanoaggregates and are generally interfacially active and can strongly adsorb to the water–oil and oil–solid interfaces, which would lead to undesirable stabilized emulsions, corrosion, and fouling of the production facilities, and even pipeline plugging [75,76].

The adsorption of asphaltenes at the water–oil interface can alter the interfacial tension, rheology, elasticity, and viscosity; therefore, the understanding of the interfacial properties of asphaltenes and their influence on the stabilization and destabilization mechanisms of emulsions are of practical significance in heavy oil industries. Shi et al. [77,78] investigated the stabilization mechanisms of asphaltenes for the O/W and W/O emulsions through the drop probe AFM technique. The nanomechanical interactions between two oil droplets in aqueous media, or two water droplets in organic solutions were directly quantified.

As illustrated in Fig. 8(a), the effect of interfacial asphaltenes on the interactions between two oil droplets can be quantified using the oil drop probe AFM technique by varying the water chemistry (i.e., pH and salinity) [77]. The involved interaction mechanisms are illustrated in Fig. 8(b). It was found that the interaction forces between two pure oil droplets in the absence of asphaltenes can be well described by the DLVO theory, and coalescence could occur in 100 mmol·L<sup>-1</sup> NaCl (Fig. 8(c)). The calculated profiles of the oil droplets just before coalescence are shown in Fig. 8(e). Under the same aqueous conditions but with the presence of asphaltenes, additional repulsion could be detected, preventing the coalescence of the oil droplets (Figs. 8(d) and (f)), which was attributed to the steric repulsion arising from the interfacial asphaltenes. The Alexander–de Gennes (AdG) model was used to describe the steric repulsion observed:

$$\Pi_{\text{steric}}(h) \approx \frac{kT}{s^3} \left[ \left( \frac{2L}{h} \right)^{9/4} - \left( \frac{h}{2L} \right)^{3/4} \right] \text{ for } D < 2L \quad (7)$$

where  $\Pi_{\text{steric}}(h)$  represents the repulsive pressure originating from the steric interaction,  $s$  is the average distance between the interfacial asphaltene molecule anchoring sites, and  $L$  is the brush length. By including the asphaltenes steric repulsion into the theoretical calculation for the disjoining pressure, the fitting of the measured force curve appears to be reasonable (Fig. 8(d)). During the separation of the two oil droplets, interfacial adhesion was occasionally observed, suggesting that the behavior of the interfacial asphaltenes was more complex than described by the AdG model. Besides, it was found that lowering pH could weaken the repulsion between the oil droplets due to the reduced negative surface potential. Ca<sup>2+</sup> was found to cause oil droplet coalescence by disrupting the interfacial asphaltene films possibly through the bridging interactions with functional groups such as carboxyl on asphaltene molecules.

As shown in Fig. 9(a), the interaction forces between two water droplets in oil (i.e., toluene) with and without interfacially adsorbed asphaltenes was measured by using the water drop probe AFM technique [78]. Without the interfacially adsorbed

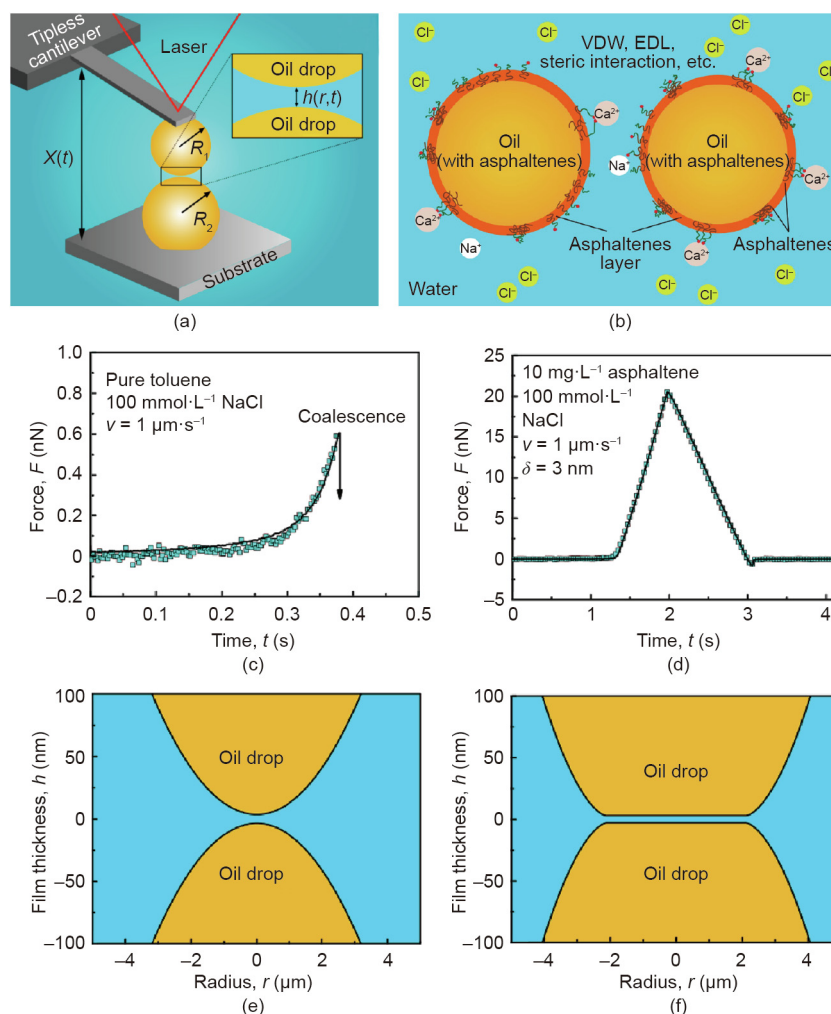


**Fig. 8.** (a) Schematic of the oil drop probe AFM setup for force measurements between two oil droplets in an aqueous medium. (b) Underlying interaction mechanisms between the oil droplets in aqueous solution with interfacially adsorbed asphaltenes. (c), (d) Typical force curves and (e), (f) the calculated droplet profiles under the maximum loading force between two oil droplets (i.e., toluene) (c), (e) without asphaltenes and (d), (f) with  $10 \text{ mg}\cdot\text{L}^{-1}$  asphaltene, in  $100 \text{ mmol}\cdot\text{L}^{-1}$  NaCl aqueous solutions. In (c) and (d), the solid curves represent the theoretical fitting results and the blue square symbols represent the experimental results. Reproduced from Ref. [77] with permission of American Chemical Society, ©2016.

asphaltenes, water droplets in toluene could readily coalesce (Fig. 9(b)). With the water droplets being aged in toluene solutions containing asphaltenes ( $10 \text{ mg}\cdot\text{L}^{-1}$ ) for 5 min in advance, coalescence could be effectively inhibited (Fig. 9(c)) and strong repulsion was detected during the approaching of the two water droplets in toluene, which was due to the steric repulsion of interfacial asphaltenes. During the separation, a “jump-out” behavior (adhesion) was observed between the two water droplets. These interaction behaviors were different from the interactions between two solid surfaces coated with asphaltenes, where adhesion was only observed in a poor solvent, e.g., heptane [79,80]. This difference was attributed to the higher mobility of asphaltenes at the oil/water interface than that on a solid surface. Thus, the asphaltenes at the oil/water interfaces were more prone to change their conformations, aggregate, and interpenetrate, thereby inducing the observed adhesion during the water droplet separation. The measured adhesion was found to first increase with higher amount of interfacial asphaltenes, then decrease when the asphaltenes amount increased further, which was attributed to the low mobility of the aggregated asphaltenes. Fig. 9(d) shows the irregular force curve between two water droplets being aged for 15 min in  $50 \text{ mg}\cdot\text{L}^{-1}$  asphaltenes solution. The measured adhesion was lower than that between water droplets with 5 min aging time. The inset

in Fig. 9(d) clearly showed tiny droplets and particles around the aged water droplets, which should be the asphaltenes aggregates. Heptol is a mixture of heptane and toluene, in which heptane is a poor solvent for asphaltenes. As shown in Fig. 9(e), increasing the heptane ratio in Heptol was found to enhance the adhesion between water droplets aged in asphaltene–toluene solution with relatively low asphaltenes concentration ( $10 \text{ mg}\cdot\text{L}^{-1}$ ), whereas it weakened the adhesion for the case aged with relatively high asphaltenes concentration ( $50 \text{ mg}\cdot\text{L}^{-1}$ ). The interfacial asphaltenes layer could be disrupted by lateral shearing and hence the coalescence could occur. Later on, the surface interactions between water droplets in pentol (i.e., mixture of pentane and toluene) were further investigated, and the effect of salt (NaCl) and asphaltenes was investigated by Xie et al. [81]. These studies systematically investigated the factors affecting the stability of both O/W and W/O emulsions with asphaltenes as the model interface-active reagent and characterized the underlying interaction mechanisms. Furthermore, the implications are useful for a wide range of stabilized O/W and W/O emulsions in various engineering processes.

The stubborn adsorption and buildup of oil foulants, especially asphaltenes, on fine mineral solids, reservoir solids, and pipelines could undermine the oil production and also increase the difficulty in tailings water treatment. Therefore, the assembly behavior of

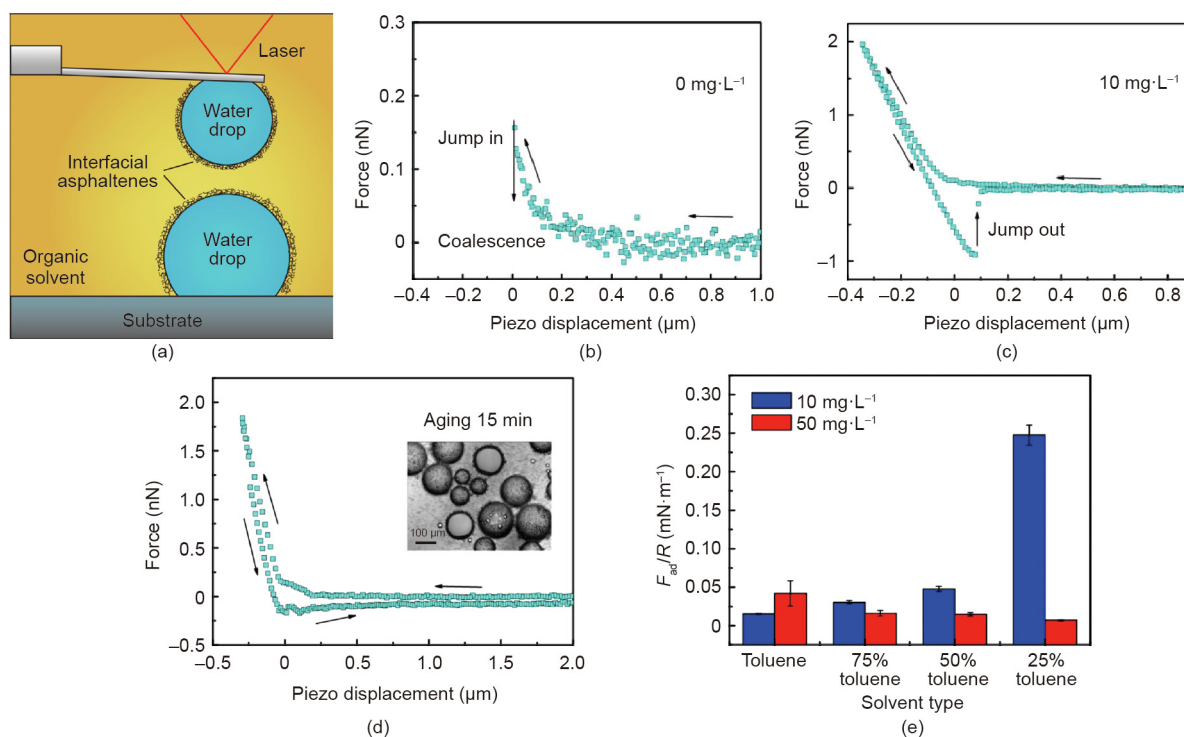


**Fig. 9.** (a) Schematic for surface force measurements between two water droplets with interfacially adsorbed asphaltenes in toluene by using the water bubble probe AFM technique. Force curves measured between two water droplets in toluene after being aged in (b)  $0 \text{ mg}\cdot\text{L}^{-1}$  and (c)  $10 \text{ mg}\cdot\text{L}^{-1}$  asphaltenes toluene solution for 5 min. (d) Force curve measured between two water droplets (radii:  $\sim 60 \mu\text{m}$ ) in toluene after being aged in  $50 \text{ mg}\cdot\text{L}^{-1}$  asphaltenes solution for 15 min. The inset photo shows the typical aged water droplets in  $50 \text{ mg}\cdot\text{L}^{-1}$  asphaltenes solution for 15 min. (e) Normalized adhesion measured between two water droplets in Heptol (i.e., mixture of toluene and heptane) after being aged in 10 and  $50 \text{ mg}\cdot\text{L}^{-1}$  asphaltenes toluene solutions. Reproduced from Ref. [78] with permission of American Chemical Society, ©2017.

asphaltenes and their conformations on solid surfaces in both oil and water were investigated [75,76]. The interaction forces between asphaltenes-coated solid surfaces were measured by using SFA and AFM [76]. By using SFA, long-range repulsion was observed between the two asphaltenes-coated solid surfaces in aqueous solution ( $1 \text{ mmol}\cdot\text{L}^{-1}$  NaCl solutions, pH 8.5, Figs. 10(a) and (c)), which could not be described by the classical DLVO theory. This phenomenon was mainly ascribed to the steric repulsion due to the formation of pancake-like patterns on the asphaltene coatings in water as confirmed by the AFM topological imaging (Fig. 10(b)). In contrast, the measured force curve between a silicon nitride AFM tip and asphaltene surface under the same aqueous condition ( $1 \text{ mmol}\cdot\text{L}^{-1}$  NaCl and pH 8.5) was measured by using AFM, and the force profile could be well fitted by the DLVO theory, suggesting that the interactions between solid substrates and asphaltenes at nanoscale mainly originated from DLVO forces.

The interactions between asphaltenes-coated surfaces in Heptol solvents were investigated by using SFA with different toluene/*n*-heptane ratios (Fig. 11(a)) [75]. In all cases, repulsion was measured during the approaching of the two asphaltenes surfaces due to the steric repulsion. It was found that the force curves could not be well fitted by one single fitting using the AdG model in the whole distance range, while they could be reasonably fitted separately in two compression regimes (Fig. 11(b)). During the surface separation, no adhesion was measured in pure toluene, while increasing the heptane weight fraction gradually increased the adhesion due to the decreased steric repulsion in increasingly poor solvent conditions (Fig. 11(c)). These results have improved the fundamental understanding on the intermolecular and surface interactions of asphaltenes and provide useful insights into modulating the stability of O/W or W/O emulsions and asphaltenes-coated solid particle suspensions in oil production processes.

Furthermore, to address the fouling issue of asphaltenes on pipelines and other facilities, the development of anti-oil fouling and self-cleaning coatings on solid substrates are highly demanded. Strong long-range attraction was discovered between water droplets and polyelectrolyte surfaces in oil as quantified using the water drop probe AFM [84]. The attraction between water droplet and polyelectrolytes was found to be stronger than that between water droplet and cationic or anionic polyelectrolytes. Such long-range attraction was proposed to be mainly attributed to the dipolar interaction between the water droplets and polyelectrolytes with large dipole moments. For molecules with high polarity, the VDW interaction energy is mainly dependent on the dipolar term  $C_{\text{orient}}$  for the Keesom orientation interaction,  $C_{\text{orient}} = -(u_1^2 u_2^2) / [3(4\pi\epsilon_0\epsilon)^2 kT]$  where  $u$  represents dipole moment. The dipole moment of the zwitterionic groups on poly(3-[dimethyl(2-methacryloyloxyethyl) ammonium] propanesulfonate) (PMAPS) was estimated as  $\sim 25 \text{ D}$  ( $1 \text{ D} \approx 3.33564 \times 10^{-30} \text{ C}\cdot\text{m}$ ), which was much stronger than those of the small molecules. For example, the dipole moment of a water molecule is  $1.85 \text{ D}$ . Thus, the VDW interaction energy between water and PMAPS in non-polar oil could be very strong, about two orders of magnitude higher than that between two small molecules. Inspired by the long-range attraction between water and PMAPS in oil and the outstanding anti-fouling performance of PMAPS, a facile and scalable strategy has been developed for the fabrication of PMAPS-polydopamine (PDA) coating [82]. For the first time, the as-prepared coating, after being fouled by oil containing asphaltenes without being prewetted by water, demonstrated superior regenerable underwater self-cleaning performance (Fig. 12(a)). Later on, superhydrophilic core-shell  $\text{Fe}_3\text{O}_4\text{@PDA-PMAPS}$  microspheres (FPPMs) were used for destabilizing W/O emulsions [83]. The as-prepared FPPM were found to facilitate the destabilization of

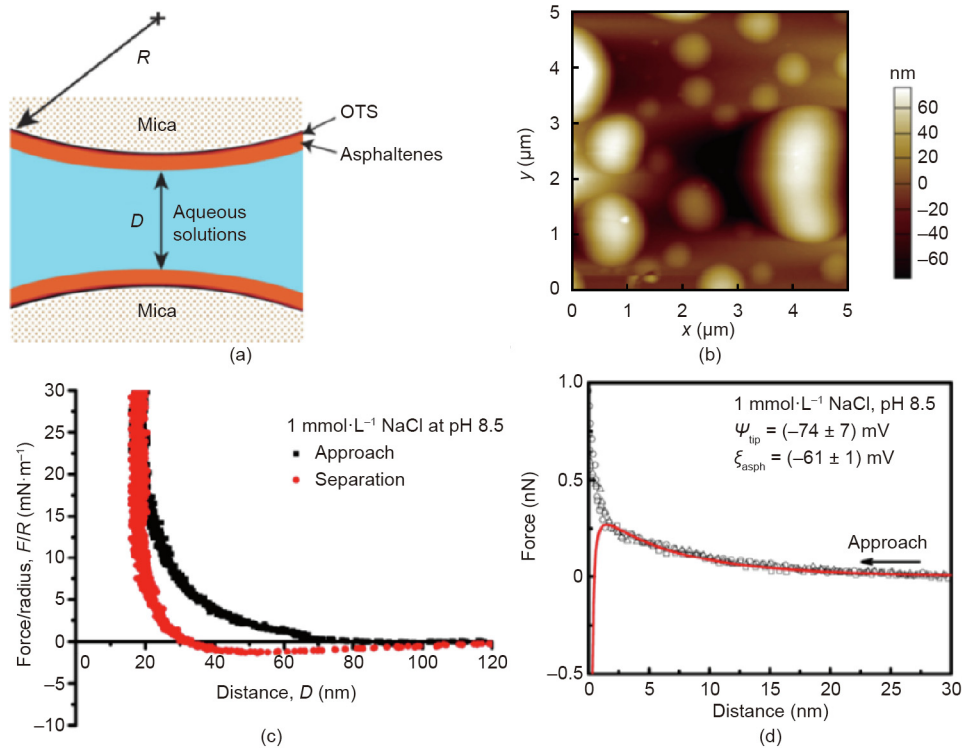


**Fig. 10.** (a) Schematic of SFA force measurements between asphaltene-coated mica surfaces in aqueous solutions. (b) AFM topological image of asphaltene surface coated on mica in aqueous solution (1 mmol·L<sup>-1</sup> NaCl, pH 8.5). (c) Force–distance profiles measured between two asphaltene surfaces interacting in 1 mmol·L<sup>-1</sup> NaCl solution at pH 8.5. (d) Force–distance profiles measured between a silicon nitride AFM tip and asphaltene surface in 1 mmol·L<sup>-1</sup> NaCl at pH 8.5. Reproduced from Ref. [76] with permission of American Chemical Society, ©2017.

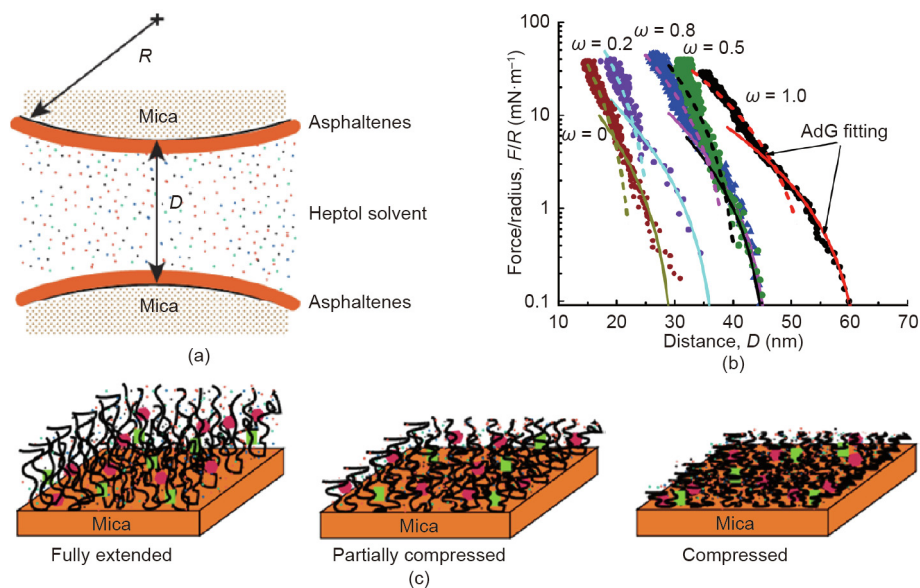


**Fig. 11.** (a) Schematic of SFA experiments measuring the interaction forces between asphaltene-coated surfaces in Heptol solvents. (b) Force–distance curves between two interacting asphaltene surfaces in pure toluene ( $\omega = 1$ ), Heptol with varying toluene weight fraction ( $\omega = 0.8, 0.5$ , and  $0.2$ ), and pure *n*-heptane ( $\omega = 0$ ). The dashed and solid lines are the theoretic fitting curves using AdG model in higher and lower compression regimes, respectively. (c) Schematic of conformations of asphaltene surfaces in toluene, Heptol, and *n*-heptane from the left to right. Reproduced from Ref. [75] with permission of American Chemical Society, ©2016.

W/O emulsions in the presence of asphaltenes under an external magnetic field by placing a magnet under the glass vials (Figs. 12(b)–(d)). AFM force measurements also demonstrated a strong attraction between PMAPS surface and water droplets in oil with asphaltenes adsorbed at the oil/water interface.

Vast tailings have been generated associated with the warm water-based bitumen extraction from oil sands. The oil sands tailings ponds occupy ~220 km<sup>2</sup> of land in north Alberta, Canada. Oil sands tailings after the initial settling become aqueous suspensions of concentrated fine solids, which are highly stable with a small



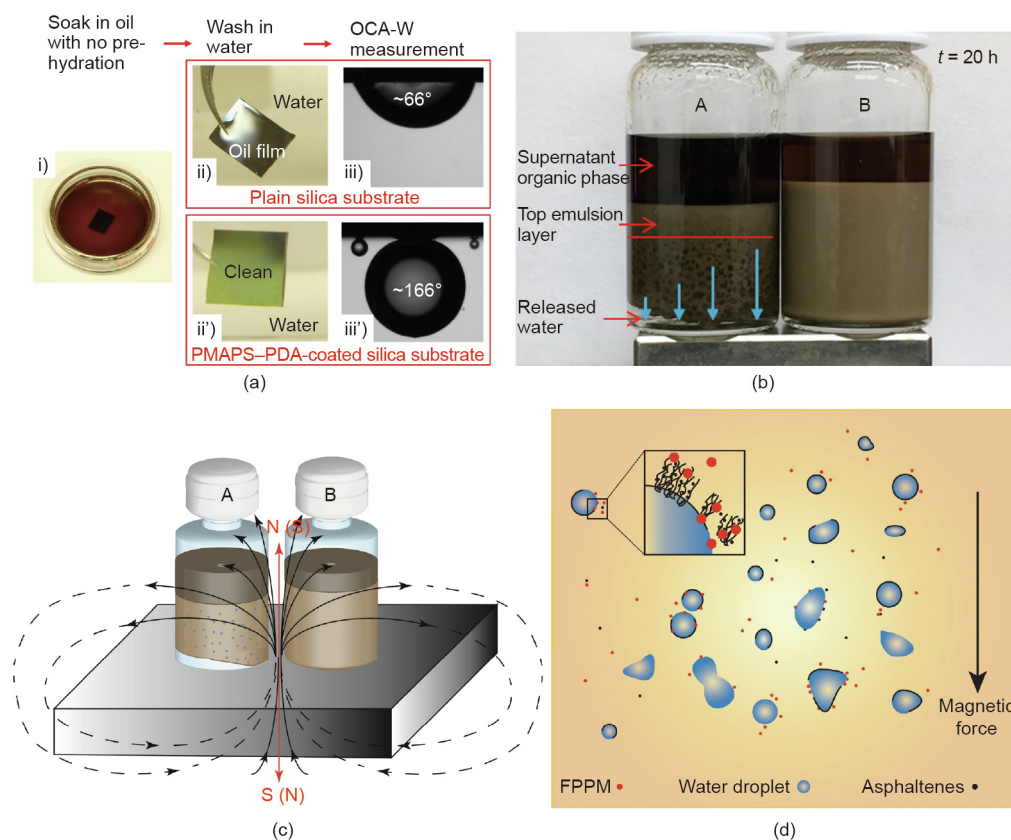


**Fig. 12.** (a) Illustrative procedure for testing the underwater self-cleaning performance of PMAPS–PDA coated on a flat silica substrate, compared with that of a plain silica substrate. The fouling oil is a model heavy oil containing asphaltenes. (b) Photograph showing the settlement of W/O emulsions (with asphaltenes) after 20 h with the addition of (A) 1 mL of FPPM suspended in toluene ( $3 \text{ mg}\cdot\text{mL}^{-1}$ ) and (B) 1 mL pristine toluene. A magnet is placed under the glass vials to apply an external magnetic field. (c) Illustration of the demulsifying settlement experiments and (d) proposed demulsification mechanisms with the addition of FPPM under external magnetic field. OCA-W: oil contact angles in water. (a) Reproduced from Ref. [82] with permission of The Royal Society of Chemistry, ©2018; (b)–(d) reproduced from Ref. [83] with permission of Elsevier, ©2018.

amount of bitumen residue [85,86]. Rapid water release from the oil sands tailings and the consolidation are challenging. Flocculation by polymer additives has shown effectiveness in tailings treatment and attracted much attention [87,88]. However, the use of a single polymer flocculant faces difficulty in simultaneously enhancing the settlement rate of the solid particles in the tailings suspensions and maintaining the clarity of released water. A two-step flocculation process was developed for the treatment of oil sands tailings by sequentially adding anionic Magnafloc-1011 (MF, a partially hydrolyzed polyacrylamide) followed by cationic chitosan, resulting in both high initial settling rate and excellent clarity of the supernatant (Fig. 13(a)) [89]. Surface force measurements using SFA showed that MF could adsorb on mica surfaces (model mineral with similar surface chemistry to silica and the major fine clays in the tailings) (Fig. 13(b)), while chitosan could lead to weak bridging between mica surfaces (Fig. 13(c)) [89,90]. In contrast, strong adhesion ( $F_{ad}/R \sim 31 \text{ mN}\cdot\text{m}^{-1}$ ) was measured between the MF-coated surfaces by adding chitosan in the confined solution (Fig. 13(d)), suggesting strong bridging effect of chitosan between MF-coated solid surfaces.

Mature fine tailings (MFTs) are a kind of extremely stable slurry, which are formed after the oil sands extraction tailings settled for a period of time (e.g., months to years). Under compression, MFT cannot hold together and thus the trapped water becomes very difficult to release. This challenge has been tackled by reinforcing MFT suspensions through polymer networks and consolidation by the subsequent filtration and mechanical compression to achieve rapid water release (Fig. 14(a)) [91]. The underlying mechanisms were substantiated by the SFA force measurements

(Fig. 14(b)). With cationic hyperbranched poly(ethyleneimine) (BPEI) added between mica surfaces, moderate adhesion ( $4.8 \text{ mN}\cdot\text{m}^{-1}$ ) was observed during the surface separation, which was attributed to the electrostatic interaction between the cationic BPEI and negatively charged mica surface. With the further addition of dibenzylaldehyde-functionalized poly(ethylene oxide) (DFPEO), the adhesion was significantly enhanced to  $12.3 \text{ mN}\cdot\text{m}^{-1}$ , which was ascribed to the formed crosslinking through Schiff base reaction between the benzylaldehyde groups in DFPEO and amine groups in BPEI. These polymers could significantly reinforce the suspensions. As demonstrated in Fig. 14(c), when the container was inverted, the MFT hydrogel composite could hold its own weight. The inset in Fig. 14(c) schematically demonstrated the interaction mechanisms among BPEI, DFPEO, and clay particles. After the mixing and treatment with polymers for about 30 min, the water released from the MFT hydrogel composite during the filtration was transparent (Fig. 14(d)) with a solid content as low as 5 ppm. The strong bonding formed in the MFT hydrogel composite endowed the composite outstanding mechanical property, allowing the filtered cake to be mechanically compressed to further squeeze out the remaining water. By using a homemade pressing system, after 1 h of compression, the volume of the filtered cake shrank to less than one third of its original volume (Fig. 14(e)). After consecutive filtration and compression, the total net water release was higher than 80%. These studies demonstrated how molecular force measurements could be correlated to the treatment of oil sands tailings containing concentrated fine solids for efficient solid–water separation. It should be noted that tailings containing concentrated colloidal solids are widely

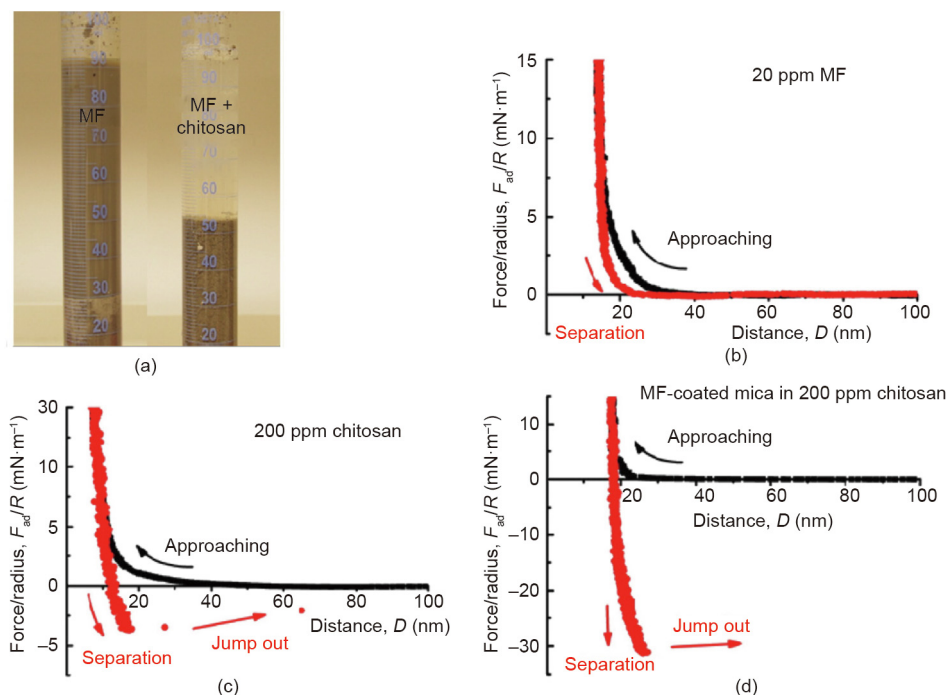


**Fig. 13.** (a) Photograph of the settled extraction tailings from oil sands production: The left one is treated by 20 ppm of MF, and the right one is treated through two-step addition of 20 ppm of MF and then 200 ppm of chitosan. Force–distance curves between mica surfaces in (b) 20 ppm of MF and (c) 200 ppm of chitosan solutions. (d) Force–distance curve between two MF-coated mica surfaces in 200 ppm of chitosan solution. Reproduced from Ref. [89] with permission of Elsevier, ©2016.

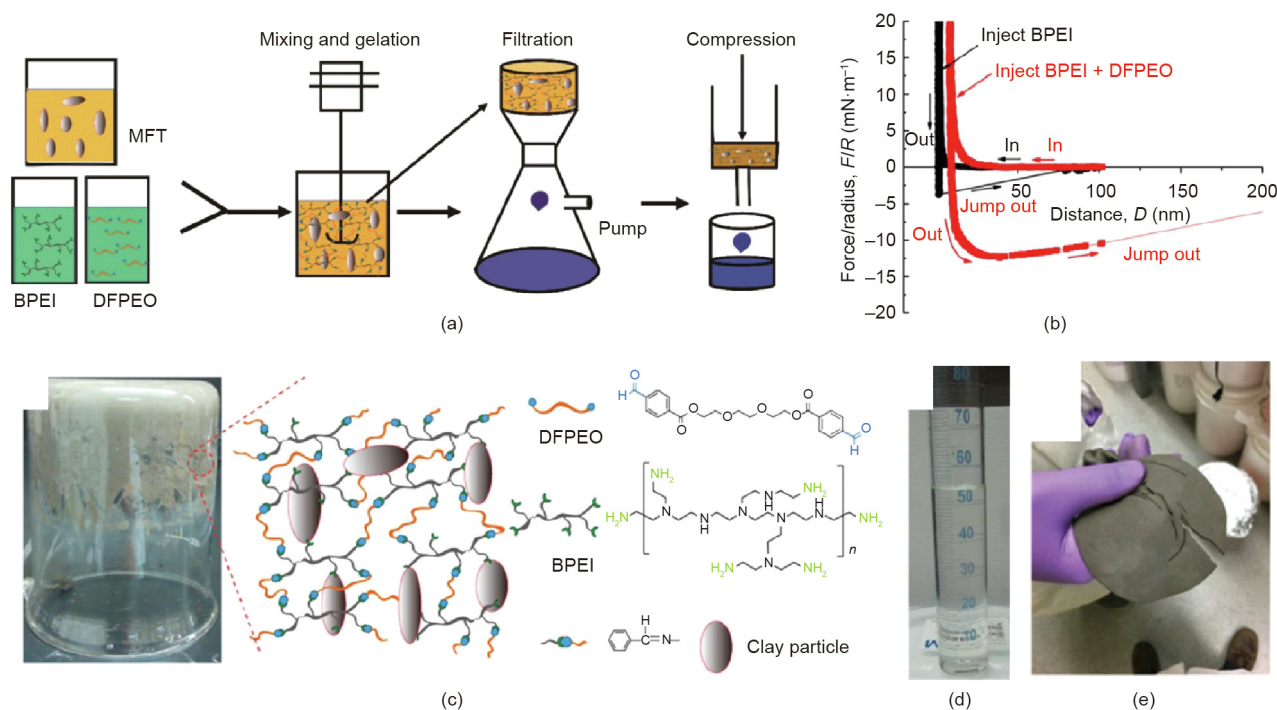


**Fig. 14.** (a) Schematic of the dewatering and consolidation procedure of the MFT suspension by sequential gelation, filtration, and compression of the MFT suspension. (b) Force–distance curves between two mica surfaces in aqueous solution after the injection of hyperbranched poly(ethylenimine) (BPEI) solution and the subsequent injection of dibenzylaldehyde-functionalized poly(ethylene oxide) (DFPEO) solution. (c) Photograph of the inverted beaker containing MFT hydrogel composite which can hold its own weight. The inset shows the schematic illustration of the interaction mechanisms. Photographs of (d) the filtrate collected 30 min after the mixing and (e) the filtered cake from 120 g of MFT after 1 h of compression (2 MPa). Reproduced from Ref. [91] with permission of American Chemical Society, ©2019.

produced in not only petroleum industry but also many other industrial processes such as mineral and food processing, and leather production. Thus, the intermolecular and surface force

measurement methodologies can be readily applied to decipher the underlying interaction mechanisms in water recovery from tailings generated in a wide variety of engineering processes, and

such studies can provide useful implications and guidance in designing functional materials and new treatment technologies [92–94].

### 4.3. Wastewater treatment

With the rapid development of modern technologies and industries, massive industrial effluents are produced daily, which contain various pollutants that need to be eliminated before the discharge to meet the water quality standards and minimize the threats to environment and creatures. Organic contaminants are one class of the major pollutants that can potentially endanger the health of creatures and ecosystems. Common organic pollutants include pesticides, pharmaceuticals, dyes, plasticizers, and fire retardants [95]. Adsorption has been demonstrated as a facile and effective treatment method for the removal of the organic contaminants from wastewater. Though many characterization techniques at the macroscopic scale have been applied to investigate the adsorption mechanisms of the organic pollutants on various adsorbents, the fundamental understanding of associated intermolecular interaction mechanisms is still limited.

Single-molecule force spectroscopy (SMFS) is a technique for direct quantification of the interaction forces at a single-molecule level, which shows great promise in investigating the intermolecular interaction between organic pollutants and adsorbents [96,97]. For example, the nanomechanical interaction mechanisms between a model organic pollutant molecule and the adsorbent, graphene oxide (GO), was directly quantified by using SMFS on an AFM [98]. As a typical cationic dye, methylene blue (MB) was used as the model aromatic organic pollutant, and GO is a novel 2-dimensional nanomaterial with high surface area and rich functional groups, which has received tremendous attention in wastewater treatment as adsorbent for the removal of various pollutants [99]. The setup of a typical SMFS experiment using AFM is illustrated in Fig. 15(a). The toluidine blue O (TBO) dye molecule

was used to mimic the chemical structure of MB with an additional amine group to be chemically tethered to one end of polyethylene glycol (PEG) (Fig. 15(b)). The other end of PEG was linked to the AFM tip, which was used as a spacer to isolate the TBO contribution from the AFM tip contribution in the measured forces [96]. In a typical single-molecule force measurement, the AFM tip was first driven to approach the GO surface deposited on the substrate, during which the TBO molecule could form physical bond with the surface of GO, and then the tip was retracted with the formed bond dissociated. Fig. 15(c) shows the typical force–extension curve during the retraction of AFM tip, which first exhibits an elastic extension of the PEG spacer and then reaches a maximum corresponding to the bond dissociation force between TBO and GO. The single-molecule force measurements were performed across different regions on the GO surface at pH 2 and 5.6 to obtain the histograms of bond dissociation forces. The representative bond dissociation force histograms at pH 2 and 5.6 are shown in Figs. 15(d) and (e), respectively. The most probable bond dissociation forces between TBO and GO were acquired by Gaussian fittings of the primary peaks (red curves). Furthermore, by fitting the most probable bond dissociation forces as a function of  $\ln(\text{loading rates}, r)$  at pH 2 and 5.6 (shown in Figs. 15(f) and (g), respectively), the activation Gibbs energy of bond dissociation ( $\Delta G$ ) and the bond dissociation distance from the equilibrium position ( $\Delta x$ ) were obtained by using the Bell-Evans model:

$$F = \frac{kT}{\Delta x} \ln\left(\frac{\Delta x}{k_0 kT}\right) + \frac{kT}{\Delta x} \ln(r) \tag{8}$$

$$\Delta G = \bar{R}T \ln(k_0/A) \tag{9}$$

where  $k_0$  represents the spontaneous bond dissociation rate, and  $\bar{R}$  represents the gas constant. The calculated  $\Delta G$  and  $\Delta x$  at pH 2 and pH 5.6 were very close, suggesting the same type of interactions corresponding to the primary peak in the bond dissociation force histograms. At pH 2, the carboxylic groups on GO are electrically

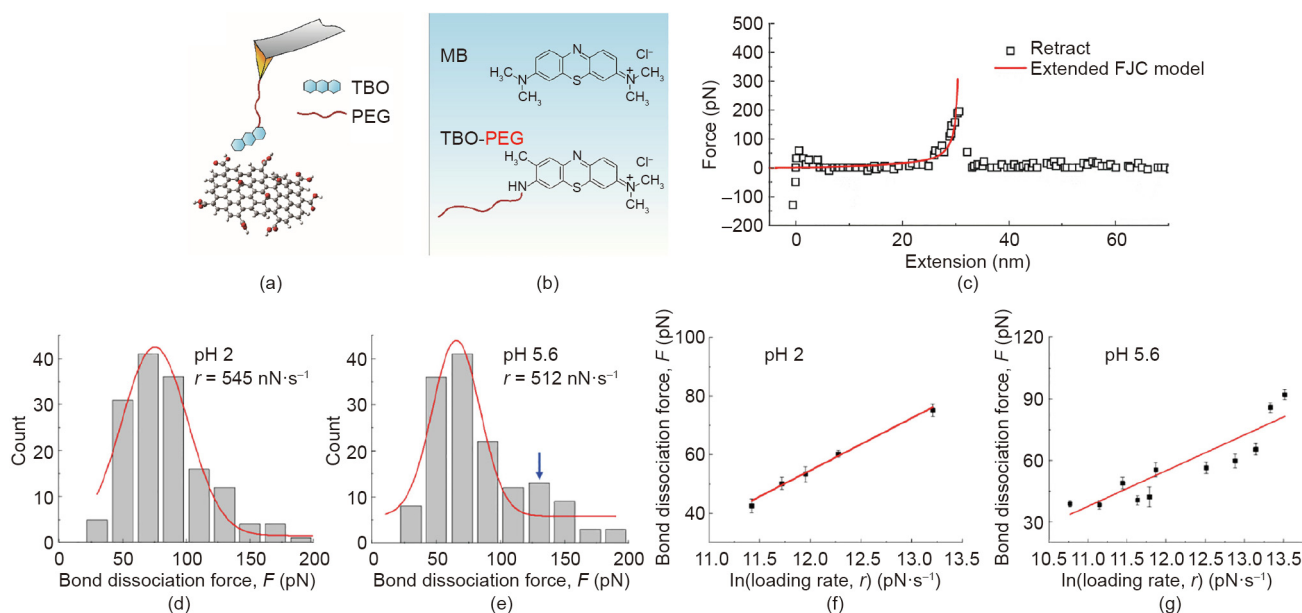


**Fig. 15.** (a) Schematic setup of a typical single-molecule force measurement to study the interaction between cationic dye molecule and GO. A single molecule of toluidine blue O (TBO), mimicking the chemical structure of MB (a commonly used organic dye), is end-tethered to the polyethylene glycol (PEG) spacer. The other end of the PEG spacer is grafted to the AFM tip. (b) Chemical structures of TBO-PEG and MB. (c) A typical force–extension curve obtained in the single-molecule force measurements during the retraction of AFM tip, which shows the typical elastic extension behavior of the PEG spacer and the force maximum indicating the bond dissociation force between TBO and GO. Representative TBO–GO bond dissociation force histograms at (d) pH 2 and (e) pH 5.6. The red curves represent the Gaussian fitting giving the most probable bond dissociation forces. The most probable bond dissociation forces between GO and TBO as a function of  $\ln(\text{loading rate}, r)$  at (f) pH 2 and (g) pH 5.6. The red lines correspond to the fitting using the Bell–Evans model. FJC: freely-jointed chain. Reproduced from Ref. [98] with permission of Elsevier, ©2018.



neutral, thus the electrostatic interaction between GO and the cationic dye should be very weak. Therefore, the bond dissociation behaviors responsible for the primary peaks of the histograms at both pH 2 and 5.6 should not be attributed to the electrostatic interaction between TBO and the carboxylic groups on GO. Furthermore, based on the complementary simulations, the primary peaks on the bond dissociation force histograms were attributed to the interactions between MB molecule and the regions on GO with epoxy groups. It was found that at pH 5.6, besides the primary peak (Fig. 15(e)), there was an additional secondary maximum in the histogram compared with that at pH 2, which was ascribed to the bond dissociations corresponding to the electrostatic interaction between the negatively charged carboxylic groups and cationic dye. As such, the important role of epoxy groups on GO for the adsorption of cationic dye pollutants was demonstrated, which was overlooked previously and could be difficult to be discovered by using the traditional macroscopic characterization techniques.

Besides adsorption, forward osmosis (FO) filtration is another technique that shows advantages in wastewater treatment due to its effectiveness, low fouling propensity, and cost. The FO treatment is a process to separate water from the dissolved pollutants by using a semi-permeable membrane, which is driven by the

osmotic pressure gradient. The FO process showed high water recovery and heavy metal rejection for the treatment of oil sands process water (OSPW) in a previous study [101]. The OSPW are the effluents chronically produced by the oil sand industries, which accumulate in the tailing ponds and require urgent remediation. Due to the tremendous amount of OSPW to be treated, the concentrated naphthenic acids (NAs) in OSPW could still lead to membrane fouling and lower the FO treatment efficiency. Thus, the interaction mechanisms between the commonly used membranes and the major functional groups in NAs (i.e., hydroxyl, carboxylic, and methyl groups) in aqueous solutions were systematically investigated by using SFA (Fig. 16(a)) [100]. Cellulose triacetate FO (CTA-FO) and aquaporin FO (AQP-FO) membranes were chosen as the model FO membranes. The reverse osmosis membrane using polyamide as the substrate (PA-RO) was chosen as the model comparison membrane that was commercially available. During the approaching of the two opposing surfaces (coated with membrane film and modified with functional groups in NAs, respectively), repulsion was observed in all SFA force measurements and the approaching (move-in) force curves could be well fitted by the DLVO model. The force–distance curves between the AQP-FO membrane surface and OH-mica, COOH-mica, and CH<sub>3</sub>-mica

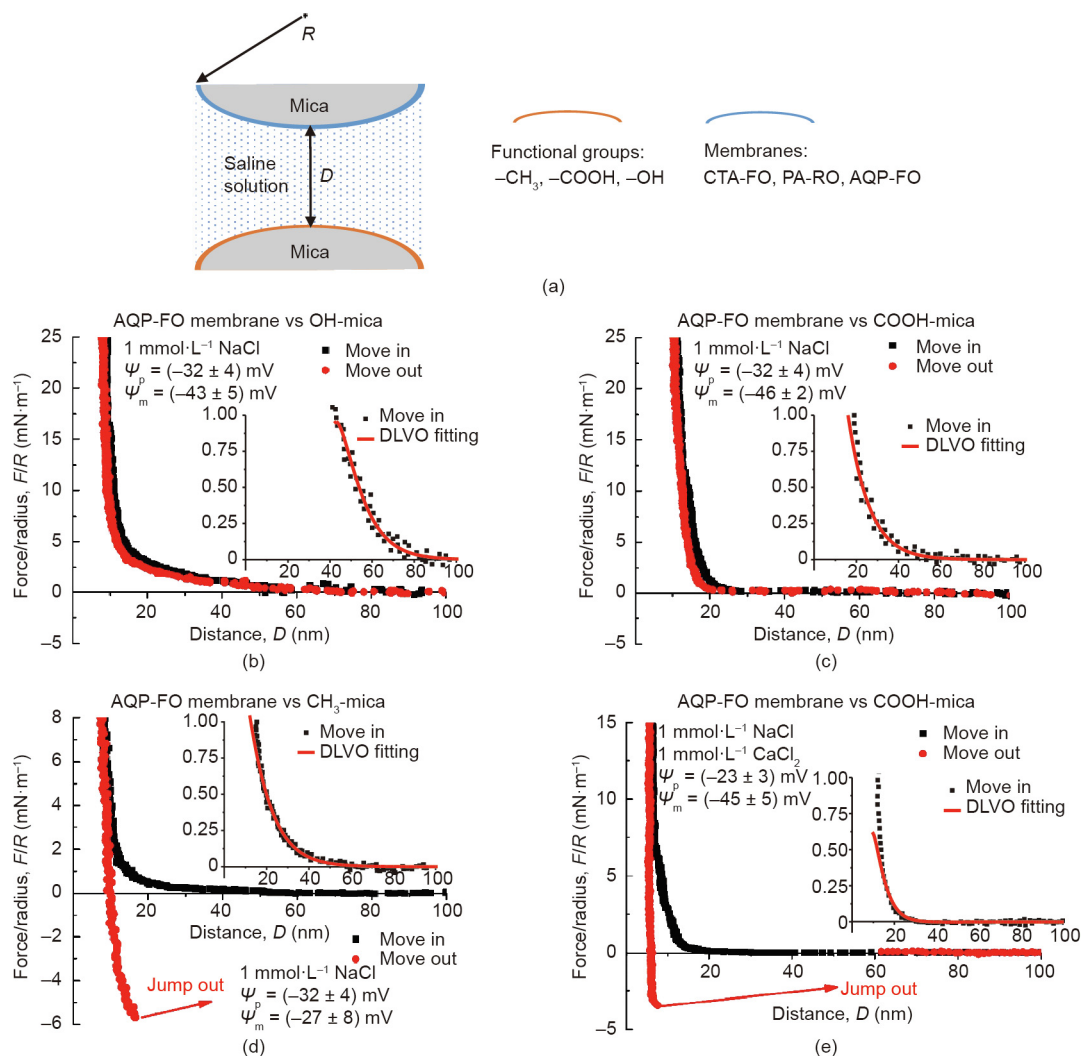


**Fig. 16.** (a) Schematic of typical SFA force measurements between functional group modified mica surfaces and membrane films coated on mica in aqueous solutions. Force–distance profiles in 1 mmol·L<sup>-1</sup> NaCl (pH 9) between aquaporin (AQP)-FO membrane surface and (b) OH-mica surface, (c) COOH-mica surface, and (d) CH<sub>3</sub>-mica surface, respectively. (e) Force–distance profile between AQP-FO membrane surface and COOH-mica surface in aqueous solution with 1 mmol·L<sup>-1</sup> NaCl and 1 mmol·L<sup>-1</sup> CaCl<sub>2</sub> (pH 9). CTA: cellulose triacetate; PA: polyamide. Reproduced from Ref. [100] with permission of Elsevier, ©2019.



surfaces are selectively shown in Figs. 16(b)–(d). Based on the Lifshitz theory, the Hamaker constants were obtained, and the VDW interaction was found to be always attractive. Through the theoretic fitting by using the DLVO model, the surface potentials of the membrane-film-coated mica surfaces ( $\psi_p$ ) and the functional group modified mica surfaces ( $\psi_m$ ) were obtained as shown in Figs. 16(b)–(d) and consistent with the reported values in literature [102–105]. The calculated Debye lengths and the negative surface potentials suggested that the long-range EDL interaction should be the main contributor for the measured repulsion during the approaching and separation of the two opposing surfaces. It should be noted that during the surface separation between the three different membrane films-coated on mica and CH<sub>3</sub>-mica surface, adhesion was observed, which followed the order of AQP-FO > CT A-FO > PA-RO. The adhesion magnitude trend was found to be consistent with the hydrophobicity trend of the membrane films coated on mica: AQP-FO > CTA-FO > PA-RO. The effect of Ca<sup>2+</sup> on the interaction forces between the three different membrane film-coated mica surfaces and COOH-mica surface was also investigated. Adhesion was only observed between the AQP-FO membrane surface and COOH-mica surface (Fig. 16(e)) due to the ion bridging effect. As such, it was demonstrated that the EDL repulsion dominated the anti-fouling performance of FO membranes for NA foulings, and the hydrophobic interaction and Ca<sup>2+</sup> bridging effect could lead to membrane fouling. The results of the batch adsorption tests and OSPW fouling experiments agreed with the SFA force results, showing the promise of using SFA in fundamentally understanding the adsorption and anti-fouling processes involved in wastewater treatment and other related engineering applications. The proposed intermolecular and surface interaction mechanisms can further provide guidance for the development of novel adsorbents and anti-fouling membranes.

#### 4.4. Energy storage materials

With the rapidly rising demand of vehicles powered by electricity, the design and fabrication of clean and sustainable energy storage systems, such as batteries and electrochemical capacitors, are highly demanded. The development of energy storage appliances with improved features including long life span, high energy, and power density are unprecedentedly challenging [106–108]. Among the energy storage systems, lithium-ion batteries show great promise due to high energy density, and the intercalation-type silicon

(Si) emerges as one of the most promising candidates as the anodic material with high theoretical specific capacity and low discharge voltage [109–112]. However, Si suffers from its high volume change during charge/discharge cycles which could lead to anode damage and decreased battery cycling life [112,113]. The use of binders together with Si particles to construct a self-healing electric network in the Si anode provides a possible solution to address this challenging issue and increase the cyclic stability [112,113]. Therefore, the understanding and investigation of the self-healing mechanisms of the electric network and the adhesion between the binders and Si are essential in designing Si anodes with high performance and long life span.

Han et al. [113] developed a liquid metal (LM)/Si nanocomposite with spontaneous repairing property, which was applied as the anode for a lithium-ion battery and showed high capacity utilization and cyclic stability (Fig. 17(a)). Due to the fluidity and self-healing nature of LM, its presence kept the integrity of the anode and the contact between the conducting network and Si particles. As shown in Fig. 17(b), during the first lithiation process, the Si particles were supposed to expand and breach the native shell of the LM droplets, thus the exposed inner LM would wet the Si surface, then the LM/Si nanocomposite was formed. AFM force measurement was performed by using a silicon nitride AFM tip to investigate the underlying surface interaction mechanisms between Si and LM in air. As shown in Fig. 17(c), during the approaching of the AFM tip, after jumping to the LM surface due to VDW interaction, the AFM tip was driven to further compress the LM surface. When the applied force achieved ~58 nN, the breakthrough of the LM shell was observed and the AFM tip touched the inner LM. During the retraction of the AFM tip, strong adhesion was measured, which was supposed to improve the intimate contact between LM and Si, ensuring the mechanical integrity and maintaining the electrical conduction in spite of the high-volume change of Si particles. The AFM force measurement directly quantified the value of the external force to break the native shell of LM, and also provided fundamental insights on the surface interaction mechanisms between Si particles and LM, guiding the future design of high-performance anode composites for lithium-ion batteries.

Zhang et al. [112] utilized a self-healing supramolecular polymer to fabricate a quadruple-hydrogen-bonded binder to be applied in Si anode, and the as-prepared anode incorporated in lithium-ion battery demonstrated high discharge capacity,

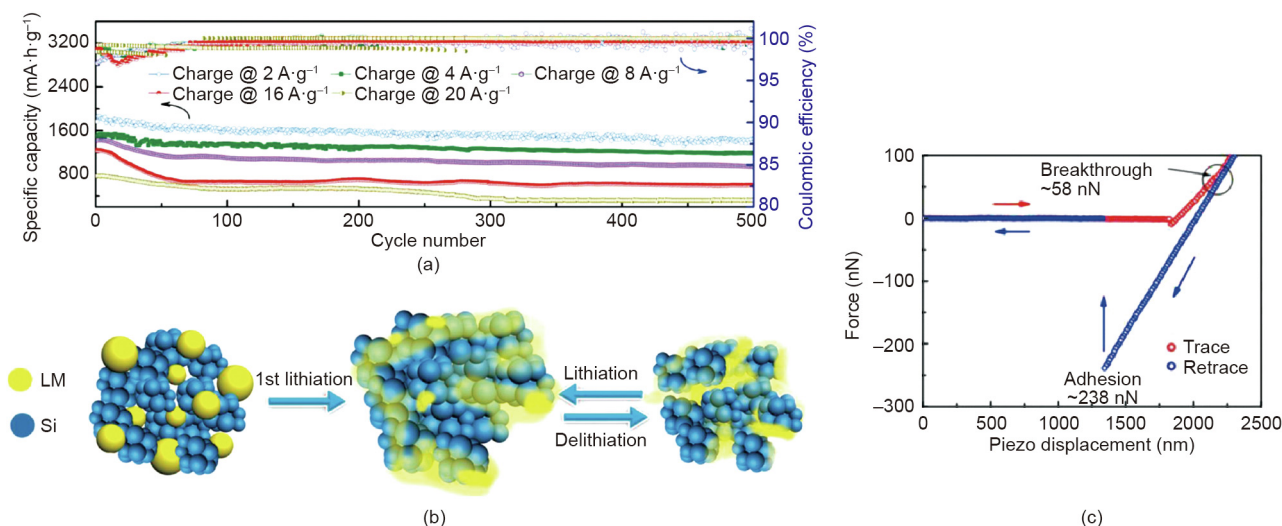
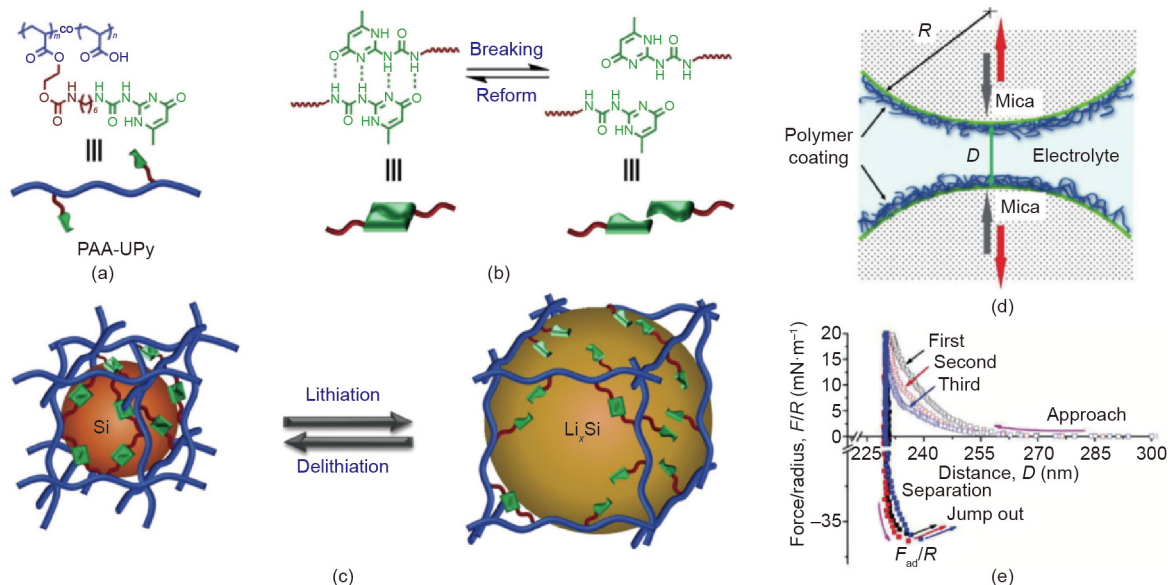


Fig. 17. (a) Cycling stability of the LM/Si anode with different current density (500 cycles). (b) Schematic illustration of the proposed charging–discharging process of the LM/Si anode. (c) Force–distance curve between a silicon nitride AFM tip (radius: 8 nm) and LM surface. Reproduced from Ref. [113] with permission of Elsevier, ©2018.



**Fig. 18.** (a) Chemical structure of supramolecular polymer composed of linear poly(acrylic acid) (PAA) integrated with ureido-pyrimidinone (UPy) moieties. (b) The breaking and reforming of UPy dimmers. (c) The dissociation and rebuilt of hydrogen bonding crosslinkings of UPy dimmers during the lithiation and delithiation processes, respectively. (d) Schematic of experimental setup for surface force measurements between polymer binders using SFA. (e) Force–distance curves obtained from three consecutive SFA force measurements. Reproduced from Ref. [112] with permission of John Wiley & Sons, ©2018.

Coulombic efficiency, and cyclic stability. As shown in Fig. 18(a), the supramolecular polymer is composed of linear poly(acrylic acid) (PAA) integrated with ureido-pyrimidinone (UPy) moieties. Stable and reversible quadruple-hydrogen bonding could form between the UPy units (Fig. 18(b)), endowing the binder with self-healing property that could ensure the cyclic stability of the as-prepared anode during the lithiation–delithiation cycles (Fig. 18(c)). The self-healing property and molecular interactions of PAA-UPy were further characterized through the SFA measurements (Fig. 18(d)). Reversible adhesion ( $F_{ad}/R \sim 36 \text{ mN}\cdot\text{m}^{-1}$ ) was observed during the three consecutive approach–separation force measurement cycles, which was attributed to the formed hydrogen bonding, and the interdigitation and interpenetration of the polymer chains, proving the self-healing capability of PAA-UPy polymers. With increasing contact time between the two PAA-UPy surfaces under compression, increased adhesion was measured through the SFA force measurements. This methodology can be extended to investigate the interaction mechanisms between polymer binder and other active materials in battery (e.g., lithium polysulfide in lithium–sulfur batteries) and provide useful implications in novel battery design.

### 5. Conclusions and perspectives

The comprehensive understanding of the intermolecular and surface interaction mechanisms in engineering processes can provide important insights into the improvement of production technologies and development of advanced functional materials (Fig. 19). In this review, our recent advances in the applications of force measurement techniques, such as AFM and SFA, in investigating the nanomechanical interactions involved in several engineering systems have been reviewed, including mineral flotation, petroleum engineering, wastewater treatment, and energy storage materials.

In mineral flotation, the selective bubble attachment on desired mineral particles treated with interface-active reagents is a critical key process. The interaction force measurements between air bubbles and a series of solid surfaces, for example, mica and  $\text{MoS}_2$ , by

using the bubble probe AFM technique have been reviewed [57,63,64,66,71,72]. The combination of RICM with the bubble probe AFM technique enables the simultaneous observation of the interaction forces between the bubbles and functionalized mica surfaces, as well as the profiles of the confined thin liquid films between them [63]. It was demonstrated that the experiment results agreed well with the theoretical calculations based on the Stokes–Reynolds–Young–Laplace equation by including the effect of disjoining pressure. Using the bubble probe AFM technique and theoretical calculations, the interaction forces and the underlying mechanisms between air bubbles and a series of mineral surfaces were investigated with varying surface hydrophobicity and water chemistry (i.e., salinity and pH, addition of interface-active polymer, and hydrodynamic condition) [57,64,66,71]. The force measurement results provide useful insights into not only for the mineral flotation process, but many other engineering processes involving the interactions between gas bubbles and solid surfaces

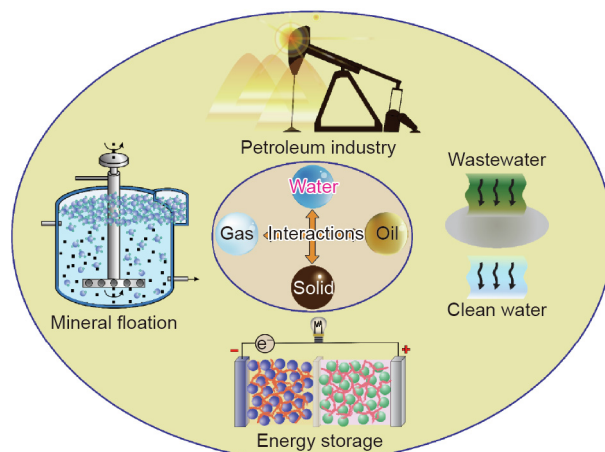


**Fig. 19.** Schematic of intermolecular and surface interactions involved in various engineering processes.

such as bitumen extraction [63,66,69]. The investigation of the interactions between the conditioning agents and mineral surfaces by quantifying the adhesion forces between the conditioning agent functionalized AFM tip and mineral surfaces have also been reviewed [73,74]. Particularly, the probing of surface interactions and *in situ* topographic information of the electrochemically active surfaces was realized by using the tip probe AFM technique with the implementation of an electrochemical setup, providing insightful implications in modulating various interfacial processes where electrochemical reactions are involved, such as colloidal stability in flotation process [59].

In petroleum engineering, the interaction forces between oil droplets in water and water droplets in oil have been directly measured and analyzed to better understand the stabilization and destabilization of O/W and W/O emulsions by using the drop probe AFM technique [77,78,81]. The effects of asphaltenes, water chemistry, and oil solvent variety were investigated. The steric repulsion originating from asphaltenes was described by using the AdG model. The fouling and assembly behaviors of asphaltenes on solid surfaces in both aqueous and oil media were surveyed by SFA and AFM. Combined with the AdG model fitting, useful insights were gained to modulate the stability of O/W and W/O emulsions as well as asphaltene-coated particle suspensions. Besides, a long-range attraction was discovered between water droplets and a polyzwitterionic surface by using the water drop probe AFM technique, which inspired the fabrication of anti-fouling polyzwitterionic coatings for underwater self-cleaning of the stubborn asphaltene-related oil fouling, and polyzwitterionic microspheres for the destabilization of W/O emulsions in the presence of asphaltenes [82–84]. The settlement and dewatering mechanisms of oil sands tailings with the assistance of polymer additives were characterized by using SFA to investigate the effect of polymers on the interactions between solid surfaces, and the measured strong adhesion could explain the excellent settlement and dewatering performance [89,91]. The correlation between the interaction forces and practical material performances/applications in different engineering processes were well demonstrated, and the unravelled interaction mechanisms provide useful guidance for resolving the practical challenges.

In wastewater treatment, SMFS was used to directly measure the interaction force between organic pollutants and adsorbents to provide useful information on the bond dissociation forces and energies [98]. The force measurement results with complementary theoretical simulations provide insightful information about the interaction mechanisms between the organic pollutants and adsorbents at a molecular scale. The fouling mechanisms of membranes were investigated by using SFA, and the role of different functional groups in the fouling molecules was studied [114]. The force measurement results were consistent with the fouling experiments and batch adsorption tests, demonstrating the importance of intermolecular and surface force measurements in improving the fundamental understanding of the adsorption and anti-fouling mechanisms involved in wastewater treatment, and further providing guidance in the design of advanced functional materials. In energy storage systems, the intermolecular and surface interactions between binders and anodic materials, and the self-healing mechanisms of their composites were investigated by using AFM and SFA, which provide useful insights into the design and development of high-performance anode composites for energy storage [112,113].

It is noted that the quantitative measurements of intermolecular and surface forces are commonly performed in relatively simple systems, for example, binary bubble–solid and drop–drop interactions. Due to the complexity of practical engineering systems with the coexistence of gas bubbles, liquid droplets, solid particles, and chemical additives in the fluid surroundings, in the future, the

intermolecular and surface force measurements should be extended to more realistic and complex systems, such as Pickering emulsions. Another technical challenge is to investigate the intermolecular and surface interactions in harsher environmental conditions (e.g., high temperature, elevated pressure, highly corrosive solutions). These harsh conditions are commonly encountered in practical industrial processes, which could influence the physical/chemical properties of the involved interacting media, thus substantially affecting their interaction forces and mechanisms. Besides, considering the irregular shape of solid particles and random roughness of substrate surfaces involved in practical engineering processes, the influence of these parameters (e.g., particle shape, surface roughness) on the related colloidal interactions should be systematically investigated.

In future studies, computational simulations and surface-sensitive spectroscopy can be combined with the force measurement techniques to provide useful information of molecule orientations and assembly behaviors, and their effects on the intermolecular and surface forces involved in various engineering processes. The established nanomechanical tools and experimental methodologies can be readily extended to many other engineering processes, for example, emulsion polymerization and oriented bubble transport. The discovered intermolecular and surface interaction principles will be correlated to the performances and practical applications of related engineering processes, providing guidance to the development of new technologies and advanced materials.

## Acknowledgements

We gratefully acknowledge the financial support from the Natural Sciences and Engineering Research Council of Canada (NSERC), the Future Energy Systems under the Canada First Research Excellence Fund (CFREF), the Canada Foundation for Innovation (CFI), and the Canada Research Chairs Program (H. Zeng).

## Compliance with ethics guidelines

Jiawen Zhang and Hongbo Zeng declare that they have no conflict of interest or financial conflicts to disclose.

## References

- [1] Zeng H. Polymer adhesion, friction, and lubrication. Hoboken: John Wiley & Sons; 2013.
- [2] Shen LG, Lei Q, Chen JR, Hong HC, He YM, Lin HJ. Membrane fouling in a submerged membrane bioreactor: impacts of floc size. *Chem Eng J* 2015;269:328–34.
- [3] Liu XM, Sheng GP, Yu HQ. DLVO approach to the flocculability of a photosynthetic H<sub>2</sub>-producing bacterium, *Rhodospseudomonas acidophila*. *Environ Sci Technol* 2007;41(13):4620–5.
- [4] Shen L, Wang X, Li R, Yu H, Hong H, Lin H, et al. Physicochemical correlations between membrane surface hydrophilicity and adhesive fouling in membrane bioreactors. *J Colloid Interface Sci* 2017;505:900–9.
- [5] Li R, Lou Y, Xu Y, Ma G, Liao BQ, Shen L, et al. Effects of surface morphology on alginate adhesion: molecular insights into membrane fouling based on XDLVO and DFT analysis. *Chemosphere* 2019;233:373–80.
- [6] Leckband D, Israelachvili J. Intermolecular forces in biology. *Quart Rev Biophys* 2001;34(2):105–267.
- [7] Wang J, Li J, Xie L, Shi C, Liu Q, Zeng H. Interactions between elemental selenium and hydrophilic/hydrophobic surfaces: direct force measurements using AFM. *Chem Eng J* 2016;303:646–54.
- [8] Israelachvili JN. Intermolecular and surface forces. 3rd ed. New York: Academic Press; 2011.
- [9] Huang J, Yan B, Faghihnejad A, Xu H, Zeng H. Understanding nanorheology and surface forces of confined thin films. *Korea–Aust Rheol J* 2014;26(1):3–14.
- [10] Dyson HJ, Wright PE, Scheraga HA. The role of hydrophobic interactions in initiation and propagation of protein folding. *Proc Natl Acad Sci USA* 2006;103(35):13057–61.
- [11] Xie L, Shi C, Wang J, Huang J, Lu Q, Liu Q, et al. Probing the interaction between air bubble and sphalerite mineral surface using atomic force microscope. *Langmuir* 2015;31(8):2438–46.



- [12] Christenson HK, Claesson PM. Direct measurements of the force between hydrophobic surfaces in water. *Adv Colloid Interface Sci* 2001;91(3):391–436.
- [13] Meyer EE, Rosenberg KJ, Israelachvili J. Recent progress in understanding hydrophobic interactions. *Proc Natl Acad Sci USA* 2006;103(43):15739–46.
- [14] Israelachvili J, Pashley R. The hydrophobic interaction is long range, decaying exponentially with distance. *Nature* 1982;300(5890):341–2.
- [15] Beattie JK, Djerdjev AM. The pristine oil/water interface: surfactant-free hydroxide-charged emulsions. *Angew Chem Int Ed* 2004;43(27):3568–71.
- [16] Meyer EE, Lin Q, Israelachvili JN. Effects of dissolved gas on the hydrophobic attraction between surfactant-coated surfaces. *Langmuir* 2005;21(1):256–9.
- [17] Siretanu I, Chapel JP, Drummond C. Water-ions induced nanostructuring of hydrophobic polymer surfaces. *ACS Nano* 2011;5(4):2939–47.
- [18] Christenson HK, Claesson PM. Cavitation and the interaction between macroscopic hydrophobic surfaces. *Science* 1988;239(4838):390–2.
- [19] Palmer LA, Cookson D, Lamb RN. The relationship between nanobubbles and the hydrophobic force. *Langmuir* 2011;27(1):144–7.
- [20] Faghhihnejad A, Zeng H. Hydrophobic interactions between polymer surfaces: using polystyrene as a model system. *Soft Matter* 2012;8(9):2746–59.
- [21] Galamba N. Water's structure around hydrophobic solutes and the iceberg model. *J Phys Chem B* 2013;117(7):2153–9.
- [22] Hooper JB, Schweizer KS. Contact aggregation, bridging, and steric stabilization in dense polymer-particle mixtures. *Macromolecules* 2005;38(21):8858–69.
- [23] Shah PS, Holmes JD, Doty RC, Johnston KP, Korgel BA. Steric stabilization of nanocrystals in supercritical CO<sub>2</sub> using fluorinated ligands. *J Am Chem Soc* 2000;122(17):4245–6.
- [24] Indekeu JO, Aarts DGAL, Lekkerkerker HNW, Hennequin Y, Bonn D. Thermal fluctuation forces and wetting layers in colloid-polymer mixtures: derivation of an interface potential. *Phys Rev E* 2010;81(4 Pt 1):041604.
- [25] Hennequin Y, Aarts DGAL, Indekeu JO, Lekkerkerker HNW, Bonn D. Fluctuation forces and wetting layers in colloid-polymer mixtures. *Phys Rev Lett* 2008;100(17):178305.
- [26] Runkana V, Somasundaran P, Kapur PC. A population balance model for flocculation of colloidal suspensions by polymer bridging. *Chem Eng Sci* 2006;61(1):182–91.
- [27] Jiang HR, Wada H, Yoshinaga N, Sano M. Manipulation of colloids by a nonequilibrium depletion force in a temperature gradient. *Phys Rev Lett* 2009;102(20):208301.
- [28] Vigil G, Xu Z, Steinberg S, Israelachvili J. Interactions of silica surfaces. *J Colloid Interface Sci* 1994;165(2):367–85.
- [29] Israelachvili JN, Pashley RM. Molecular layering of water at surfaces and origin of repulsive hydration forces. *Nature* 1983;306(5940):249–50.
- [30] Trokhymchuk A, Henderson D, Wasan DT. A molecular theory of the hydration force in an electrolyte solution. *J Colloid Interface Sci* 1999;210(2):320–31.
- [31] Derjaguin BV. A theory of the heterocoagulation, interaction and adhesion of dissimilar particles in solutions of electrolytes. *Discuss Faraday Soc* 1954;18:85–98.
- [32] Derjaguin BV, Titjvskaja AS, Abricossava II, Malkina AD. Investigations of the forces of interaction of surfaces in different media and their application to the problem of colloid stability. *Discuss Faraday Soc* 1954;18:24–41.
- [33] Rentsch S, Pericet-Camara R, Papastavrou G, Borkovec M. Probing the validity of the Derjaguin approximation for heterogeneous colloidal particles. *Phys Chem Chem Phys* 2006;8(21):2531–8.
- [34] Neuman KC, Nagy A. Single-molecule force spectroscopy: optical tweezers, magnetic tweezers and atomic force microscopy. *Nat Methods* 2008;5(6):491–505.
- [35] Zhang L, Xie L, Cui X, Chen J, Zeng H. Intermolecular and surface forces at solid/oil/water/gas interfaces in petroleum production. *J Colloid Interface Sci* 2019;537:505–19.
- [36] Gong L, Xiang L, Zhang J, Chen J, Zeng H. Fundamentals and advances in the adhesion of polymer surfaces and thin films. *Langmuir* 2019;35(48):15914–36.
- [37] Zhang X, Ma L, Zhang Y. High-resolution optical tweezers for single-molecule manipulation. *Yale J Biol Med* 2013;86(3):367–83.
- [38] Dulin D, Cui TJ, Nossen J, Docter M, Lipfert J, Dekker N. High Spatiotemporal-resolution magnetic tweezers: calibration and applications for DNA dynamics. *Biophys J* 2015;109(10):2113–25.
- [39] Sarkar R, Rybenkov VV. A guide to magnetic tweezers and their applications. *Front Phys* 2016;4:48.
- [40] Tabor D, Winterton RHS. The direct measurement of normal and retarded van der Waals forces. *Proc R Soc Lond A* 1969;312(1511):435–50.
- [41] Israelachvili JN, Tabor D. The shear properties of molecular films. *Wear* 1973;24(3):386–90.
- [42] Israelachvili JN, Tabor D. Measurement of van der Waals dispersion forces in the range 1.4 to 130 nm. *Nat Phys Sci* 1972;236(68):106.
- [43] Israelachvili J, Min Y, Akbulut M, Alig A, Carver G, Greene W, et al. Recent advances in the surface forces apparatus (SFA) technique. *Rep Prog Phys* 2010;73(3):036601.
- [44] Zeng H, Tian Yu, Zhao B, Tirrell M, Israelachvili J. Friction at the liquid/liquid interface of two immiscible polymer films. *Langmuir* 2009;25(9):4954–64.
- [45] Maeda N, Chen N, Tirrell M, Israelachvili JN. Adhesion and friction mechanisms of polymer-on-polymer surfaces. *Science* 2002;297(5580):379–82.
- [46] Zeng H, Maeda N, Chen N, Tirrell M, Israelachvili J. Adhesion and friction of polystyrene surfaces around T<sub>g</sub>. *Macromolecules* 2006;39(6):2350–63.
- [47] Zeng H, Tian Y, Anderson TH, Tirrell M, Israelachvili JN. New SFA techniques for studying surface forces and thin film patterns induced by electric fields. *Langmuir* 2008;24(4):1173–82.
- [48] Kristiansen K, Zeng H, Zappone B, Israelachvili JN. Simultaneous measurements of molecular forces and electro-optical properties of a confined 5CB liquid crystal film using a surface forces apparatus. *Langmuir* 2015;31(13):3965–72.
- [49] Valtiner M, Banquy X, Kristiansen K, Greene GW, Israelachvili JN. The electrochemical surface forces apparatus: the effect of surface roughness, electrostatic surface potentials, and anodic oxide growth on interaction forces, and friction between dissimilar surfaces in aqueous solutions. *Langmuir* 2012;28(36):13080–93.
- [50] Kristiansen K, Donaldson SH Jr, Berkson ZJ, Scott J, Su R, Banquy X, et al. Multimodal miniature surface forces apparatus ( $\mu$ SFA) for interfacial science measurements. *Langmuir* 2019;35(48):15500–14.
- [51] Binnig G, Rohrer H, Gerber C, Weibel E. Surface studies by scanning tunneling microscopy. *Phys Review Lett* 1982;49(1):57–61.
- [52] Binnig GK, inventor; International Business Machines Corp, assignee. Atomic force microscope and method for imaging surfaces with atomic resolution. United States patent USRE33387E. 1990 Oct 16.
- [53] Binnig G, Quate CF, Gerber C. Atomic force microscope. *Phys Rev Lett* 1986;56(9):930–3.
- [54] Ducker WA, Senden TJ, Pashley RM. Direct measurement of colloidal forces using an atomic force microscope. *Nature* 1991;353(6341):239–41.
- [55] Butt HJ. Electrostatic interaction in atomic force microscopy. *Biophys J* 1991;60(4):777–85.
- [56] Butt HJ, Cappella B, Kappl M. Force measurements with the atomic force microscope: technique, interpretation and applications. *Surf Sci Rep* 2005;59(1–6):1–152.
- [57] Shi C, Chan DYC, Liu Q, Zeng H. Probing the hydrophobic interaction between air bubbles and partially hydrophobic surfaces using atomic force microscopy. *J Phys Chem C* 2014;118(43):25000–8.
- [58] Dagastine RR, Manica R, Carnie SL, Chan DYC, Stevens GW, Grieser F. Dynamic forces between two deformable oil droplets in water. *Science* 2006;313(5784):210–3.
- [59] Xie L, Shi C, Cui X, Zeng H. Surface forces and interaction mechanisms of emulsion drops and gas bubbles in complex fluids. *Langmuir* 2017;33(16):3911–25.
- [60] Xing Y, Xu M, Gui X, Cao Y, Babel B, Rudolph M, et al. The application of atomic force microscopy in mineral flotation. *Adv Colloid Interface Sci* 2018;256:373–92.
- [61] Ducker WA, Xu Z, Israelachvili JN. Measurements of hydrophobic and DLVO forces in bubble-surface interactions in aqueous solutions. *Langmuir* 1994;10(9):3279–89.
- [62] Butt HJ. A technique for measuring the force between a colloidal particle in water and a bubble. *J Colloid Interface Sci* 1994;166(1):109–17.
- [63] Shi C, Cui X, Xie L, Liu Q, Chan DYC, Israelachvili JN, et al. Measuring forces and spatiotemporal evolution of thin water films between an air bubble and solid surfaces of different hydrophobicity. *ACS Nano* 2015;9(1):95–104.
- [64] Liu S, Xie L, Liu G, Zhong H, Wang Y, Zeng H. Hetero-difunctional reagent with superior flotation performance to chalcopyrite and the associated surface interaction mechanism. *Langmuir* 2019;35(12):4353–63.
- [65] Butt HJ. Measuring electrostatic, van der Waals, and hydration forces in electrolyte solutions with an atomic force microscope. *Biophys J* 1991;60(6):1438–44.
- [66] Xie L, Wang J, Yuan D, Shi C, Cui X, Zhang H, et al. Interaction mechanisms between air bubble and molybdenite surface: impact of solution salinity and polymer adsorption. *Langmuir* 2017;33(9):2353–61.
- [67] Contreras-Naranjo JC, Ugaz VM. A nanometre-scale resolution interference-based probe of interfacial phenomena between microscopic objects and surfaces. *Nat Commun* 2013;4(1):1919.
- [68] Cui X, Shi C, Xie L, Liu J, Zeng H. Probing interactions between air bubble and hydrophobic polymer surface: impact of solution salinity and interfacial nanobubbles. *Langmuir* 2016;32(43):11236–44.
- [69] Xie L, Shi C, Cui X, Huang J, Wang J, Liu Q, et al. Probing the interaction mechanism between air bubbles and bitumen surfaces in aqueous media using bubble probe atomic force microscopy. *Langmuir* 2018;34(3):729–38.
- [70] Shi C, Cui X, Zhang X, Tchoukov P, Liu Q, Encinas N, et al. Interaction between air bubbles and superhydrophobic surfaces in aqueous solutions. *Langmuir* 2015;31(26):7317–27.
- [71] Cui X, Shi C, Zhang S, Xie L, Liu J, Jiang D, et al. Probing the effect of salinity and pH on surface interactions between air bubbles and hydrophobic solids: implications for colloidal assembly at air/water interfaces. *Chem Asian J* 2017;12(13):1568–77.
- [72] Pearse MJ. An overview of the use of chemical reagents in mineral processing. *Miner Eng* 2005;18(2):139–49.
- [73] Liu S, Xie L, Liu J, Liu G, Zhong H, Wang Y, et al. Probing the interactions of hydroxamic acid and mineral surfaces: molecular mechanism underlying the selective separation. *Chem Eng J* 2019;374:123–32.
- [74] Xie L, Wang J, Shi C, Huang J, Zhang H, Liu Q, et al. Probing surface interactions of electrochemically active galena mineral surface using atomic force microscopy. *J Phys Chem C* 2016;120(39):22433–42.
- [75] Zhang L, Shi C, Lu Q, Liu Q, Zeng H. Probing molecular interactions of asphaltenes in heptol using a surface forces apparatus: implications on stability of water-in-oil emulsions. *Langmuir* 2016;32(19):4886–95.



- [76] Zhang L, Xie L, Shi C, Huang J, Liu Q, Zeng H. Mechanistic understanding of asphaltene surface interactions in aqueous media. *Energy Fuels* 2017;31(4):3348–57.
- [77] Shi C, Zhang L, Xie L, Lu X, Liu Q, Mantilla CA, et al. Interaction mechanism of oil-in-water emulsions with asphaltenes determined using droplet probe AFM. *Langmuir* 2016;32(10):2302–10.
- [78] Shi C, Zhang L, Xie L, Lu X, Liu Q, He J, et al. Surface interaction of water-in-oil emulsion droplets with interfacially active asphaltenes. *Langmuir* 2017;33(5):1265–74.
- [79] Natarajan A, Xie J, Wang S, Liu Q, Masliyah J, Zeng H, et al. Understanding molecular interactions of asphaltenes in organic solvents using a surface force apparatus. *J Phys Chem C* 2011;115(32):16043–51.
- [80] Wang S, Liu J, Zhang L, Masliyah J, Xu Z. Interaction forces between asphaltene surfaces in organic solvents. *Langmuir* 2010;26(1):183–90.
- [81] Xie L, Lu Q, Tan X, Liu Q, Tang T, Zeng H. Interfacial behavior and interaction mechanism of pentol/water interface stabilized with asphaltenes. *J Colloid Interface Sci* 2019;553:341–9.
- [82] Zhang J, Zhang L, Cui X, Gong L, Xiang L, Shi C, et al. Scalable polyzwitterion-polydopamine coating for regenerable oil/water separation and underwater self-cleaning of stubborn heavy oil fouling without pre-hydration. *Chem Commun* 2018;54(70):9734–7.
- [83] Mao X, Gong L, Xie L, Qian H, Wang X, Zeng H. Novel Fe<sub>3</sub>O<sub>4</sub> based superhydrophilic core-shell microspheres for breaking asphaltene-stabilized water-in-oil emulsion. *Chem Eng J* 2019;358:869–77.
- [84] Shi C, Yan B, Xie X, Zhang L, Wang J, Takahara A, et al. Long-range hydrophilic attraction between water and polyelectrolyte surfaces in oil. *Angew Chem Int Ed Engl* 2016;55(48):15017–21.
- [85] Swart NC, Weaver AJ. The Alberta oil sands and climate. *Nat Clim Chang* 2012;2(3):134–6.
- [86] Li SM, Leithead A, Moussa SG, Liggio J, Moran MD, Wang D, et al. Differences between measured and reported volatile organic compound emissions from oil sands facilities in Alberta, Canada. *Proc Natl Acad Sci USA* 2017;114(19):E3756–65.
- [87] Farkish A, Fall M. Rapid dewatering of oil sand mature fine tailings using super absorbent polymer (SAP). *Miner Eng* 2013;50–51:38–47.
- [88] Gray M, Xu Z, Masliyah J. Physics in the oil sands of Alberta. *Phys Today* 2009;62(3):31–5.
- [89] Lu Q, Yan B, Xie L, Huang J, Liu Y, Zeng H. A two-step flocculation process on oil sands tailings treatment using oppositely charged polymer flocculants. *Sci Total Environ* 2016;565:369–75.
- [90] Yan B, Huang J, Han L, Gong L, Li L, Israelachvili JN, et al. Duplicating dynamic strain-stiffening behavior and nanomechanics of biological tissues in a synthetic self-healing flexible network hydrogel. *ACS Nano* 2017;11(11):11074–81.
- [91] Yan B, Han L, Xiao H, Zhang J, Huang J, Hu W, et al. Rapid dewatering and consolidation of concentrated colloidal suspensions: mature fine tailings via self-healing composite hydrogel. *ACS Appl Mater Interfaces* 2019;11(24):21610–8.
- [92] Wang C, Harbottle D, Liu Q, Xu Z. Current state of fine mineral tailings treatment: a critical review on theory and practice. *Miner Eng* 2014;58:113–31.
- [93] Mezzenga R, Schurtenberger P, Burbidge A, Michel M. Understanding foods as soft materials. *Nat Mater* 2005;4(10):729–40.
- [94] Elabbas S, Ouazzani N, Mandi L, Berrekhis F, Perdicakis M, Pontvianne S, et al. Treatment of highly concentrated tannery wastewater using electrocoagulation: influence of the quality of aluminium used for the electrode. *J Hazard Mater* 2016;319:69–77.
- [95] Cameron N, Bogin B, editors. *Human growth and development*. New York: Academic Press; 2013.
- [96] Zhang Y, Liu C, Shi W, Wang Z, Dai L, Zhang X. Direct measurements of the interaction between pyrene and graphite in aqueous media by single molecule force spectroscopy: understanding the  $\pi$ - $\pi$  interactions. *Langmuir* 2007;23(15):7911–5.
- [97] Hinterdorfer P, Dufrène YF. Detection and localization of single molecular recognition events using atomic force microscopy. *Nat Methods* 2006;3(5):347–55.
- [98] Zhang J, Lu X, Shi C, Yan B, Gong L, Chen J, et al. Unraveling the molecular interaction mechanism between graphene oxide and aromatic organic compounds with implications on wastewater treatment. *Chem Eng J* 2019;358:842–9.
- [99] Zhang J, Azam MS, Shi C, Huang J, Yan B, Liu Q, et al. Poly(acrylic acid) functionalized magnetic graphene oxide nanocomposite for removal of methylene blue. *RSC Adv* 2015;5(41):32272–82.
- [100] Xiang L, Zhu S, Li M, Zhang J, El-Din MG, Zeng H. Probing fouling mechanism of naphthenic acids on forward osmosis polymer membranes in oil sands process water treatment. *J Membr Sci* 2019;576:161–70.
- [101] Jiang Y, Liang J, Liu Y. Application of forward osmosis membrane technology for oil sands process-affected water desalination. *Water Sci Technol* 2016;73(8):1809–16.
- [102] Ambrożewicz D, Ciesielczyk F, Nowacka M, Karasiewicz J, Piasecki A, Maciejewski H, et al. Fluoroalkylsilane versus alkylsilane as hydrophobic agents for silica and silicates. *J Nanomater* 2013;2013:631938.
- [103] Ding W, Cai J, Yu Z, Wang Q, Xu Z, Wang Z, et al. Fabrication of an aquaporin-based forward osmosis membrane through covalent bonding of a lipid bilayer to a microporous support. *J Mater Chem A Mater Energy Sustain* 2015;3(40):20118–26.
- [104] Pashley RM, Israelachvili JN. DLVO and hydration forces between mica surfaces in Mg<sup>2+</sup>, Ca<sup>2+</sup>, Sr<sup>2+</sup>, and Ba<sup>2+</sup> chloride solutions. *J Colloid Interface Sci* 1984;97(2):446–55.
- [105] Zhu S, Panne U, Rurack K. A rapid method for the assessment of the surface group density of carboxylic acid-functionalized polystyrene microparticles. *Analyst* 2013;138(10):2924–30.
- [106] Manthiram A, Fu Y, Chung SH, Zu C, Su YS. Rechargeable lithium-sulfur batteries. *Chem Rev* 2014;114(23):11751–87.
- [107] Miller JR. Applied physics. Valuing reversible energy storage. *Science* 2012;335(6074):1312–3.
- [108] Cui X, Zhang L, Zhang J, Gong L, Gao M, Zheng P, et al. A novel metal-organic layered material with superior supercapacitive performance through ultrafast and reversible tetraethylammonium intercalation. *Nano Energy* 2019;59:102–9.
- [109] Higgins TM, Park SH, King PJ, Zhang CJ, McEvoy N, Berner NC, et al. A commercial conducting polymer as both binder and conductive additive for silicon nanoparticle-based lithium-ion battery negative electrodes. *ACS Nano* 2016;10(3):3702–13.
- [110] Shi Y, Zhou X, Yu G. Material and structural design of novel binder systems for high-energy, high-power lithium-ion batteries. *Acc Chem Res* 2017;50(11):2642–52.
- [111] Yi H, Lan T, Yang Y, Lei Z, Zeng H, Tang T, et al. Aqueous-processable polymer binder with strong mechanical and polysulfide-trapping properties for high performance of lithium-sulfur batteries. *J Mater Chem A Mater Energy Sustain* 2018;6(38):18660–8.
- [112] Zhang G, Yang Y, Chen Y, Huang J, Zhang T, Zeng H, et al. A quadruple-hydrogen-bonded supramolecular binder for high-performance silicon anodes in lithium-ion batteries. *Small* 2018;14(29):e1801189.
- [113] Han B, Yang Y, Shi X, Zhang G, Gong L, Xu D, et al. Spontaneous repairing liquid metal/Si nanocomposite as a smart conductive-additive-free anode for lithium-ion battery. *Nano Energy* 2018;50:359–66.
- [114] Xiang L, Gong L, Zhang J, Zhang L, Hu W, Wang W, et al. Probing molecular interactions of PEGylated chitosan in aqueous solutions using a surface force apparatus. *Phys Chem Chem Phys* 2019;21(37):20571–81.